# University of Naples “Federico II”


*Department of Clinical Medicine and Surgery*

**Doctorate Program in Advanced Biomedical and Surgical Treatments – XXXIII Cycle**

Director: Prof. Giovanni di Minno

DOCTORAL THESIS

# “Nuclear FGFR1 regulates gene transcription and promotes antiestrogen resistance in ER+ breast cancer”

**MENTOR** **CANDIDATE**

Prof. Roberto Bianco, MD, PhD Alberto Servetto, MD

ACADEMIC YEAR 2019-2020

## Table of contents

# 1. Introduction

FGFR1 belongs to the family of Fibroblast Growth Factor Receptors, comprising four highly conserved transmembrane receptor tyrosine kinases (RTKs) FGFR1-4, and another membrane-associated receptor lacking the intracellular domain (FGFR5 or FGFRL1) (1). FGFRs are activated upon binding of ligands (fibroblast growth factors, FGFs) to their extracellular domain (2) followed by receptor dimerization and phosphorylation of C-terminal tyrosines. These phosphorylated tyrosines dock several adaptor proteins that induce activation of downstream signaling pathways, including RAS/RAF/MEK/ERK, PI3K/AKT, PLCγ and STATs (3-6).

The genomic locus of *FGFR1*, 8p11-12, is amplified in various cancer types, including breast, lung, ovarian and bladder tumors (7-10). *FGFR1* gene amplification has been identified in about 15% of patients with ER+ breast cancers (11). We have previously shown that *FGFR1* gene amplification is associated with resistance to estrogen suppression in a cohort of patients with ER+ breast cancer treated with the aromatase inhibitor letrozole (12).

The oncogenic role of FGFR1 is generally the result of genomic aberrations, such as gene amplification, activating mutations, gene fusions, or by dysregulated autocrine/paracrine signaling, involving FGF ligands (13). In addition to the canonical intracellular signaling function of membrane-bound FGFR1, there is experimental evidence that FGFR1 can localize in the nucleus of cancer cells (14,15). The role of nuclear FGFR1 has been investigated in the context of neuronal development. In embryonic stem cells (ESCs), nuclear FGFR1 has been shown to interact with chromatin, alone or in association with the nuclear receptors RXR (Retinoid X Receptor) or NR4A1 (also known as Nur77 or nerve growth factor IB), thereby promoting gene transcription associated with developmental pathways (16). Furthermore, in human medulloblastoma cells, FGFR1 interacts with CREB-Binding Protein (CBP) and ribosomal S6 kinase 1 (RSK1) in the nucleus. In this ternary complex, FGFR1 induces CBP-mediated transcription by releasing CBP from RSK1 inhibition and directly activating CBP (17).

There is a growing body of evidence showing that RTKs, in addition to their signal transduction function as membrane-bound receptors, can also be found in the nucleus (18). For example, it

was recently reported that the Insulin Receptor (IR) associates with several gene promoters, thus regulating gene expression profiles involved in classic insulin-related functions (19). Genomic binding studies recently identified a direct involvement of HER2 (ERBB2) in gene transcription regulation in *HER2*-amplified breast cancers (20). Other studies showed that EGFR binds to promoters of genes involved in cancer cell proliferation and regulates their expression (21).

FGFR1 overexpression has been associated with resistance to antiestrogen therapy in ER+ breast cancers (22,23). We previously showed that estradiol deprivation in patients resulted in a significant increase in both cytosolic and nuclear FGFR1 levels in ER+/*FGFR1*-amplified breast cancer cells in primary tumors (24). In this study, we now report abundant levels of FGFR1 in nuclear and chromatin-bound fractions from ER+/*FGFR1*-amplified PDXs as well as a correlation between nuclear localization of FGFR1 and resistance to estrogen suppression in ER+ primary tumors in patients. Hence, we have examined whether nuclear FGFR1 has a potential causal role in endocrine resistance. To investigate a transcriptional function of nuclear FGFR1, we analyzed genome-wide chromatin occupancy of FGFR1 by chromatin immunoprecipitation followed by next-generation sequencing (ChIP-Seq) and FGFR1-associated gene expression profiles by RNA sequencing (RNA-seq) in ER+/*FGFR1*-amplified breast cancer cells. Taken together, these analyses identified a functional role for nuclear FGFR1 in transcriptional regulation, driving gene expression associated with antiestrogen resistance and poor patient outcome.

## 2. Materials and Methods

**Cell lines and inhibitors:** MCF-7 (ATCC® HTB-22™), CAMA1 (ATCC® HTB-21™), and MDA-MD-134-VI (ATCC® HTB-23™) human breast cancer cells were obtained from the American Type Culture Collection (ATCC) and maintained in ATCC-recommended media supplemented with 10% FBS (Gibco) and 1× antibiotic/antimycotic (Gibco) at 37°C in a humidified atmosphere of 5% $CO_2$ in air. Cell lines were authenticated by ATCC prior to purchase by the short tandem repeat (STR) method. All experiments were performed <2 months after thawing early passage cells. Mycoplasma testing was conducted for each cell line before use. Fulvestrant, tamoxifen and erdafitinib were purchased from Selleck Chemicals.

**Xenograft studies:** Mouse experiments were approved by the UT Southwestern Institutional Animal Care and Use Committee (IACUC). Female ovariectomized athymic mice (Envigo) were implanted with a 14-day-release 17β-estradiol pellet (0.17 mg; Innovative Research of America). The following day, $1 \times 10^7$ MCF-$7^{EV}$ or MCF-$7^{FGFR1(SP-)(NLS)}$ cells suspended in PBS and Matrigel at 1:1 ratio were injected subcutaneously (s.c.) into the right flank of each mouse. Approximately 4 weeks later, mice bearing tumors measuring ≥150 $mm^3$ were randomized to treatment with vehicle (control) or fulvestrant (5 mg per week; s.c.). Tumor diameters were measured with caliper every four days and tumor volume in $mm^3$ was calculated with the formula: volume = $width^2 \times length/2$. After 4 weeks, tumors were harvested and snap-frozen in liquid nitrogen or fixed in 10% neutral buffered formalin followed by embedding in paraffin. Four-micron paraffinized sections were used for IHC using ERα (Santa Cruz Biotechnology #8002) antibody. Sections were scored by an expert pathologist (P.G.E) blinded to treatment arm.

**Immunohistochemistry**: For IHC analysis, samples were prepared as previously described (24). Briefly, formalin-fixed paraffin-embedded (FFPE), 4-µm tissue sections were deparaffinized. Antigen retrieval was performed with citrate buffer pH 6. Endogen peroxidase was blocked and protein block was applied. Sections were then incubated with FGFR1 ab10646 (Abcam) antibody at 1:2000 overnight at 4°C. The visualization system Envision (Agilent Technologies, Santa Clara, CA). DAB was used as chromogen (Agilent Technologies) and hematoxylin was applied as

counterstain. Slides were digitally acquired using an AxioScan Z1 slide scanner (Carl Zeiss) at 20x. For the results shown in figures 1B and S2B, automated semiquantitative scoring was performed on whole slide images using QuPath software (25). Color deconvolution stains were set for hematoxylin and DAB. Cell segmentation was determined on hematoxylin. An object classifier was trained to define tumor and stroma compartments. Percentage of FGFR1 positive cells over total tumor cell and H-score were calculated with the positive cell detection algorithm according to the nuclear DAB optical densities mean. Each selected region was visually assessed for correct performance of the quantification algorithm. Ki67 expression in biopsies from patients treated with letrozole prior to surgery was measured by automated quantitative immunofluorescence, as previously described (12,26).

**ChIP and reChIP assays:** Cells cultured in 15-cm dishes were washed with PBS once and incubated with serum free DMEM media containing 1% formaldehyde, for 10 min at room temperature. Crosslinking was quenched with glycine. Plates were next washed with ice-cold PBS three times and cells scraped off the plate with ice-cold PBS with protease inhibitor tablet (Mini, EDTA-free Protease Inhibitor Cocktail – ROCHE – Cat no. 04693159001). Cells were centrifuged at 720 xg for 10 min at 4°C and resuspended in 1.5 ml sonication buffer (1% SDS, 10 mM EDTA, 50 mM Tris-HCl, pH 8.0-8.1) with protease inhibitor. After rotation at 4°C for 10 min, chromatin was sonicated using a Bioruptor Plus sonication device (Diagenode) at 4°C. Sonicated chromatin was adjusted to a final concentration of 200 mM NaCl and incubated at 65°C overnight. The following day, the chromatin was incubated with RNAse A for 30 min at 37°C, followed by Proteinase K for 1 h at 42°C. DNA was purified using QIAquick PCR Purification Kit (Cat 28106). DNA shearing was checked, with an average fragment size of 200-750 bp. To conduct chromatin immunoprecipitation (ChIP), the sonicated chromatin was eluted with ChIP dilution buffer (0.01% SDS buffer, 1.1% Triton X-100, 1.2 mM EDTA, 167 mM NaCl, 16.7 mM Tris-HCl, pH 8.0-8.1) with protease inhibitors and precleared with Gammabind G Sepharose beads (GE Healthcare, Cat no. 17-0885-01) previously washed three times with ChIP-dilution buffer and preblocked in 0.5% BSA at 4°C for 1 h. The precleared chromatin was incubated at 4°C overnight with primary antibody. The following day, Gammabind G Sepharose beads were added to the antibody pulldowns for 2

h at 4°C. Next, beads were washed once in Buffer I (0.1% SDS, 1% Triton X-100, 2 mM EDTA, 20 mM Tris-HCl, 150 mM NaCl and protease inhibitors, pH 8.0-8.1), once in Buffer II (0.1% SDS, 1% Triton X-100, 2 mM EDTA, 20 mM Tris-HCl, 500 mM NaCl, and protease inhibitors), once in Buffer III (0.25 M LiCl, 1% NP40, 1% Na-deoxycholate, 1 mM EDTA, 10 mM Tris-HCl, pH 8.0-8.1) and twice in TE buffer, pH 8.0-8.1. Complexes were eluted off the beads in Elution Buffer (0.1 M NaHCO3, 1%SDS) at 65°C for 10 min, twice, in a thermomixer. Eluates from the antibody pulldowns and sonicated chromatin (as input controls) were adjusted to 200 mM NaCl and incubated at 65°C overnight. The following day, sequential incubations with RNAse A for 30 min at 37°C, and Proteinase K for 1 h at 42°C were performed. DNA was purified using QIAquick PCR Purification Kit. ChIPed and input DNA was analyzed by qRT-PCR or used to construct sequencing libraries. For ChIP-qPCR, the enrichment was shown as percent of input. ChIP-qPCR results presented in Figures 3H, 5D, 5F, S5B, S5C, S5E, S8C, S8D, S11D, S11E, were reproduced in two or more independent experiments. We used the following primary antibodies for ChIP experiments: rabbit anti-FGFR1 (Abcam, ab10646), normal rabbit IgG (Cell Signaling Technology, 2729), rabbit anti-histone H3 acetyl K27 (Abcam, ab4729), rabbit anti-histone H3 trimethyl K4 (Abcam, ab8580), mouse anti-Rpb1 CTD 4H8 (Cell Signaling Technology, 2629), mouse anti-HNF-3α (Santa Cruz Biotechnology, sc-101058). For ChIP-qPCR, primer pair sequences were designed based on the nucleotide sequences identified by ChIP-Seq peaks and derived from UCSC Genome Browser. The identified sequence was input in BLAST (Basic Local Alignment Search Tool) to design valuable pair sequences.

For reChIP, ChIP with rabbit anti-FGFR1 or normal rabbit IgG was performed as described above but after the last TE wash, beads were incubated with reChIP elution buffer (10 mM Tris pH 7.6, 1 mM EDTA, 2% SDS, 20 mM DTT) and heated at 37°C for 30 min (19). Samples were centrifuged at 1000 xg x 1 min and the supernatant was diluted 20-fold in ChIP dilution buffer containing protease inhibitors. Next, samples were split and incubated with rabbit IgG or mouse anti-HNF-3α or mouse anti-Rpb1 CTD 4H8 at 4°C overnight. The reChIP samples were collected, washed, and eluted as described above for ChIP. The enrichment value was measured by qRT-PCR and shown as percent (%) of input of the first round of ChIP**.**

**ChIP-Sequencing analysis:** Cells were cultured in 15-cm dishes and kept for 48 h in IMEM/10% Charcoal Stripped Serum (CSS) prior to apply the ChIP protocol described above. For ChIP-Seq experiment shown in figure 6F, CAMA1 cells were cultured for 24 h in serum free DMEM media, prior to treatment with FGF2 (R&D Systems, 233-FB) (5 ng/ml, 3 h) ± erdafitinib (250 nM, 3 h). All ChIP-Seq in CAMA1 cells experiments were conducted on two biological replicates. ChIP-Seq experiments in MCF7$^{FGFR1(SP-)(NLS)}$ cells were conducted on three biological replicates. Libraries from 5–10 ng ChIP DNA were prepared using KAPA Hyper Library Preparation Kit. ChIPed DNA was quantified on the Qubit® 4 Fluorometer (Invitrogen). Samples were end repaired, 3' ends adenylated and barcoded with multiplex adapters, followed by size selection with Ampure XP beads and PCR amplification. Samples were next quantified by Qubit and validated on the Agilent Tapestation 4200, normalized and pooled, and then run on the Illumina NextSeq 500 using 75 cycle SBS v2.5 reagents. Reads were aligned to human reference genome (hg38) using Bowtie2(v2.2.3)(27) with default parameters. Low quality reads and duplicate reads were removed from aligned files using "samtools view -bh -F 0x04 -q 10"(28) and "Picard MarkDuplicates.jar" (https://github.com/broadinstitute/picard) commands. Model-based Analysis of ChIP-Seq (MACS)(29) software tool (v.2.1.2) was used to identify TF bound regions from the ChIP-seq data. MACS uses 200-bp as the fragment length and each read was shifted by 100-bp to identify candidate peaks with significant tag enrichment. Default parameters of MACS were applied using an FDR cutoff of 5% to select the peaks for further analysis. For motif analysis, 200-bp around the peak region was used. *De novo* motif discovery analysis was performed using findMotifsGenome module in homer (v4.9). We used bdgcmp executable available in MACS software tools to calculate the background signal from the input sample and subtract it from the ChIP signal. We used the "ppois" method to calculate the normalized signal. To plot sequencing read densities relative to specific positions in the genome, we used annotatePeaks function available in Homer tools(30) This function takes the peak coordinates, tags directories as input and extends each tag by their estimated ChIP-fragment length, and calculates ChIP fragment coverage represented in per base pairs per peak. Heatmaps were plotted using signal density in the 5000-bp region around each peak. Density plots around TSS were plotted using ngsplot

tool(31). For results shown in figure 6C, GREAT (http://great.stanford.edu/public/html/) was used to identify the potential biological functions of the FGFR1 DNA binding sites with default parameters.

**RNA-Sequencing analysis:** For experiment in figure 2E, CAMA1 cells were cultured in 10-cm dishes in IMEM/10% CSS for 48 h. For experiment in figure 6A, CAMA1 cells were cultured for 24 h in serum free DMEM media, prior to treatment with DMSO or FGF2 (5 ng/ml, 6 h). Cells were harvested and RNA was purified using a RNA purification kit (Maxwell, Promega). Each experiment was conducted in three biological replicates. Samples were run on the Agilent Tapestation 4200 to ensure use of only high quality RNA (RIN Score ≥8). The Qubit fluorometer was used to determine sample concentration prior to preparation of libraries. One µg of total DNAse treated RNA was then prepared with the TruSeq Stranded mRNA Library Prep Kit from Illumina. Poly-A RNA was purified and fragmented before strand specific cDNA synthesis. cDNAs were then a-tailed and indexed adapters were ligated. After adapter ligation, samples were PCR amplified and purified with AmpureXP beads, then validated again on the Agilent Tapestation 4200. Before being normalized and pooled, samples were quantified by Qubit then run on the Illumina NextSeq 500 using V2.5 reagents. RNA-seq reads were mapped to human genome (hg38) and junctions were identified using tophat(v2.1.2). RNA-seq expression counts for each gene were quantified using featureCounts module from Subread package (v.1.6.3). Differential expression analysis was performed using DESeq2 (v.1.24.0) R package. Binding and Expression Target Analysis (BETA) v1.0.7, with the BETA-plus protocol, was used to evaluate significant association between FGFR1-bound genomic loci in $MCF7^{FGFR1(SP-)(NLS)}$ and differentially expressed genes in $MCF7^{EV}$ vs $MCF7^{FGFR1(SP-)(NLS)}$ cells. BETA was also used to evaluate significant association between FGFR1-bound genomic loci and FGF2-induced DEGs in CAMA1 cells. GSEA analysis were performed using a JAVA GSEA 3.0 program.

**Gene expression analysis.** RNA was extracted and purified from cells or xenografts using Maxwell RSC simplyRNA Cells Kit or simplyRNA Tissue Kit (Promega Corporation). cDNA was generated using iScript cDNA Synthesis Kit (Bio-Rad). qPCR was performed with a cDNA equivalent of 50 ng RNA, 1 mmol/L each of the forward and reverse primers, and SYBR Green

PCR Master Mix (Applied Biosystems), using a QuantStudio 3 Real-Time PCR System Machine (Applied Biosystems). All primers were purchased from QIAGEN: GAPDH (PPH00150F) PGR (PPH01007F), CCND1 (PPH00128F), VEGFA (PPH00251C), TFF1 (PPH00998C), PDZK1 (PPH08038E), CDK4 (PPH00118F), CDK12 (PPH05712A), DUSP1 (PPH00406A), FTO (PPH16000B), JUNB (PPH00179A), GREB1 (PPH20761F), MYC (PPH00100B), FOS (PPH00094A), BRD2 (PPH09948A). Ct (threshold cycle) values were determined in triplicate samples by subtracting the target gene Ct from the GAPDH Ct; $2^{-\Delta\Delta Ct}$ was used to determine the expression of selected mRNAs relative to GAPDH.

**Immunoprecipitation and western blot analysis:** Cells were seeded in 15-cm dishes and after three washes with ice-cold PBS, harvested in lysis buffer (50 mM Tris pH 7.5, 150 mM NaCl, 0.5 mM EDTA, and 1% Triton X-100) supplemented with protease inhibitors (Mini, EDTA-free Protease Inhibitor Cocktail – ROCHE) and phosphatase inhibitor (PhosSTOP; ROCHE). Lysates were sonicated using a Bioruptor Plus sonication device (Diagenode) at 4°C, at maximum power for 10 min with 30 sec on and 30 sec off twice. Lysates were incubated with DNase I (Thermo Fisher Scientific) and Benzonase (Sigma-Aldrich) at 37°C for 10 min, followed by centrifugation at 20,000 xg at 4°C for 10 min. Protein concentration in the supernatants was determined using Pierce BCA Protein Assay Reagents (Thermo Fisher). Lysates were incubated overnight with primary antibodies at 4°C and antibody pulldowns were captured by incubation with Protein G dynabeads for 2 h at 4°C. Beads were washed and the immune complexes eluted from the beads following manufacturer's instructions (Dynabeads Protein G Immunoprecipitation Kit – Thermo Fisher). Eluted proteins were separated by SDS-PAGE and transferred to nitrocellulose membranes. Membranes were blocked with 5% milk at room temperature for 1 h and then incubated overnight with primary antibodies at 4°C, followed by incubation with HRP-conjugated rabbit or mouse secondary antibodies for 1-2 h at room temperature. Protein bands were detected with an enhanced chemiluminescence substrate (Pierce ECL Western Blotting substrate, Thermo Fisher). The following primary antibodies were used for immunoprecipitation: rabbit anti-FGFR1 (Abcam, ab10646), mouse anti-FLAG M2 (Sigma-Aldrich), mouse anti-Rpb1 CTD 4H8 (Cell Signaling Technology, 2629), rabbit Phospho-Rpb1 CTD (Ser2) (E1Z3G) (Cell signaling

technology, 13499), mouse anti-CDK7 (CST, 2916), mouse anti-CDK9 (Santa Cruz Biotechnology, sc-13130), mouse anti-HNF-3α (Santa Cruz Biotechnology, sc-101058), normal rabbit IgG (CST, 2729), mouse IgG2b isotype control (CST, 53484). The following primary antibodies were used for immunoblotting: rabbit anti-FGFR1 (Abcam ad76464), mouse anti-FLAG M2 (Sigma-Aldrich), mouse anti-Rpb1 CTD 4H8 (Cell Signaling Technology, 2629), rabbit Phospho-Rpb1 CTD (Ser2) (E1Z3G) (Cell signaling technology, 13499), mouse anti-CDK7 (CST, 2916), mouse anti-CDK9 (Santa Cruz Biotechnology, sc-13130), mouse anti-HNF-3α (Santa Cruz Biotechnology, sc-101058), rabbit anti-α/β Tubulin (CST, 2148), rabbit anti-AIF (CST, 5318), mouse anti-Lamin A/C (CST, 4777), rabbit anti-Histone H3 (CST, 4499), rabbit anti-phospho-FGF Receptor (Tyr653/654) (CST, 3471), rabbit anti-phospho-FRS2α (Tyr436) (CST, 3861), rabbit anti-phospho-p44/42 MAPK (Erk1/2) (Thr202/204) (CST, 4370), rabbit anti-p44/42 MAPK (Erk1/2)(137F5) (CST, 4695), mouse anti-β-actin (CST, 3700). For immunoprecipitation followed MS, CAMA1$^{FGFR13XFLAG}$ cells underwent subcellular fractionation according to the manufacturer's protocol (Subcellular Protein Fractionation Kit for Cultured Cells, CST #78840). Soluble nuclear and chromatin-bound fractions were combined, sonicated and nuclease-treated as described above and used for immunoprecipitation with mouse anti-FLAG M2 (Sigma-Aldrich) and mouse IgG2b isotype control (CST, 53484) antibodies. For subcellular fractionation assays shown in figures 6D and S13A, CAMA1 cells were cultured for 24 h in serum free DMEM media, prior to treatment with FGF2, 5 ng/ml ± erdafitinib 250 nM for 3 h.

**Mass Spectrometry:** Immunoprecipitated proteins were separated by SDS-PAGE. Excised Gel band samples were digested overnight with trypsin (Promega) following reduction and alkylation with DTT and iodoacetamide (Sigma–Aldrich). Digests underwent solid-phase extraction cleanup with an Oasis MCX plate (Waters) followed by run on an Orbitrap Fusion Lumos mass spectrometer coupled to an Ultimate 3000 RSLC-Nano liquid chromatography system. Samples were injected onto a 75 um i.d., 75-cm long EasySpray column (Thermo). The mass spectrometer operated in positive ion mode with a source voltage of 2.2 kV and an ion transfer tube temperature of 275°C. MS scans were acquired at 120,000 resolution in the Orbitrap; up to 10 MS/MS spectra were obtained in the ion trap for each full spectrum acquired using higher-energy collisional

dissociation (HCD) for ions with charges 2-7. Dynamic exclusion was set for 20 sec after an ion was selected for fragmentation. Raw MS data files were analyzed using Proteome Discoverer v2.2 (Thermo), with peptide identification performed using Sequest HT searching against the human protein database from UniProt. Fragment and precursor tolerances of 10 ppm and 0.6 Da were specified, and three missed cleavages were allowed. Carbamidomethylation of Cys was set as a fixed modification, with oxidation of Met set as a variable modification. A false-discovery rate (FDR) cutoff of 1% was used for all peptides. We used three replicates of FLAG-immunoprecipitates and two replicates for IgG-immunoprecipitates. Only the proteins present in all three FLAG pulldown replicates and absent in IgG pulldown replicates or with a fold enrichment in FLAG over IgG >10 were considered as positive hits. Proteins with less than two peptide hits were not included.

**Immunofluorescence**. Cells were seeded in MatTek 35 mm dishes (MatTek Life Sciences) and after 48 h, fixed with 4% PFA for 30 min. Cells were next incubated in 0.25% Triton X-100 in PBS for 5 min, then in blocking buffer (10% BSA in PBS) for 60 min, followed by an overnight incubation with an FGFR1 antibody (Abcam cat #76464) at 4 °C. The following day, cells were incubated with a goat anti-rabbit IgG (H+L) cross-adsorbed secondary antibody, Alexa Fluor 488 (Thermo Fisher Scientific, cat #A-11008) for 60 min, followed by DAPI staining. Vectashield antifade mounting medium (Vector Laboratories, cat #H-1000-10) was used as mounting solution. Images were collected with a fully automated inverted microscope (DMI8, Leica microsystems). Quantification of nuclear fluorescence was performed with the software ImageJ.

***FGFR1* fluorescent *in situ* hybridization (FISH) analysis.** Four-µm tissue sections were mounted on charged slides and hybridized overnight with the SPEC *FGFR1:CEN8* Dual Color Probe (ZytoVision, catalog# Z-2072-200). Briefly, deparaffinization, protease treatment and washes were performed as per standard protocols. After this pretreatment, the slides were denatured in the presence of 10 µL of the probe for 6 min at 72°C, and hybridized at 37°C overnight in StatSpin (Thermobrite, Abbott Molecular, Inc.). Post-hybridization saline-sodium citrate washes were performed at 72°C and the slides were then stained with DAPI before analysis. Tumor tissue was scanned for amplification hot spots under 20× magnification (Olympus

BX60 Fluorescent microscope). If the *FGFR1* signals were homogeneously distributed, then random areas were used for counting the signals. Images for cell counting were captured with a 100x oil immersion objective using Cytovision software. Twenty to sixty tumor cell nuclei were individually evaluated by counting green *FGFR1* and orange centromere 8 signals. The *FGFR1:CEN8* ratio and the average *FGFR1* copy number for each specimen were calculated next. Based on HER2 guidelines (32), samples were considered to be *FGFR1* amplified under one of the following conditions: a) *FGFR1:CEN8* ratio ≥2.0; b) average number of *FGFR1*signals ≥6.

**Clonogenic assay**: For experiments in figures 1D, 1E, S3C and S3D, cells ($5 \times 10^4$/well) were seeded in triplicate in 10% DMEM-FBS in 6-well plates and treated with 0.5-10 nM fulvestrant. For experiment shown in figure S12F, $2.5 \times 10^4$ cells/well were seeded in triplicate in DMEM-FBS in 12-well plates and treated with increasing doses of erdafitinib. Seven days later, when control wells reached 50–70% confluence, monolayers were fixed and stained with 20% methanol/80% water/0.5% crystal violet for 20 min, washed with water, and dried. Photographic images of the plates were obtained. The crystal violet was solubilized with 20% acid acetic and the image intensity of the monolayers was quantified by spectrophotometric detection at 490 nm using a plate reader (GloMax®-Multi Detection System, Promega). For the experiment in figure S3E, $1 \times 10^4$ cells were seeded in 24-well plate. After 6 days of treatment, monolayers were stained with crystal violet and processed as described above.

**PDX-derived cell sorting:** HCI-011 PDXs established in ovariectomized SCID/beige mice were harvested and dissociated using digestion buffer [125 µg/mL DnaseI (#LS002138, Worthington), 10 µg/mL Dispase (#LS02109, Worthington), 500 µg/mL Collagenase 3 (#LS004182, Worthington), and 5× triple antibiotics (#15240-062, Invitrogen) in CnT-PR media (CellIntec)]. Dissociated single cells were washed with ice-cold PBS, stained with APC anti-human CD298 Antibody (Biolegend, #341706) for 30 min at 4°C, and fixed with 1% formaldehyde for 15 min at 4°C. FACS analysis was performed on the FACSAria Fusion flow cytometer (BD Biosciences). APC+ cells were collected, washed with ice-cold PBS twice and then resuspended in sonication buffer (1% SDS, 10 mM EDTA, 50 mM Tris-HCl, pH 8.0-8.1) with protease inhibitors.

**Plasmid and viral transfection:** 3XFLAG-FGFR1-expressing lentiviral constructs were generated in the pLX302 Gateway vector (Open Biosystems). To generate stably transduced CAMA1 cells, 4 µg of the 3XFLAG-FGFR1-pLX302 construct were cotransfected with 3 µg psPAX2 and 1 µg pMD2G envelope plasmid into 293FT cells using FuGENE 6 (Promega). 293FT growth media was changed 24 h post-transfection; virus-containing supernatants were harvested 48 and 72 h post-transfection, passed through a 0.45-mm filter, diluted 1:4, and applied to target cells with 8 µg/mL polybrene (Sigma Aldrich). Virus-producing cells were selected in 1 µg/mL puromycin. pCDNA3.1(-)FGFR1(SP-)(NLS) has been previously described (33). FGFR1(SP-)(NLS) genomic sequence was cloned from pCDNA3.1(-)FGFR1(SP-)(NLS) into pLVX-M-puro plasmid by restriction enzyme cloning, to generate the pLVX-M-puro-FGFR1(SP-)(NLS) plasmid. pLVX-M-puro empty vector and pLVX-M-puro-FGFR1(SP-)(NLS) plasmid were cotransfected with 3 µg psPAX2 and 1 µg pMD2G envelope plasmid into 293FT cells as described above. Virus-containing supernatants from 293FT cells were collected as described above and applied to MCF-7 cells with 8 µg/mL polybrene (Sigma Aldrich). Virus-producing cells were selected in 1 µg/mL puromycin.

**siRNA transfection:** Silencer Select pre-designed siRNAs targeting FGFR1, and FOXA1 were purchased from Ambion. Cells were reverse-transfected with siRNAs of interest using lipofectamine RNAiMAX transfection reagent (ThermoFisher Scientific) as per manufacturer's instructions. Twenty-four h post-transfection, the culture media was replaced with IMEM/10% CSS. Seventy-two h post-transfection, the ChIP or RNA extraction protocols described above were applied. Simultaneously, transfected cells were harvested in lysis buffer (50 mM Tris pH 7.5, 150 mM NaCl, 0.5 mM EDTA, and 1% Triton X-100) for protein extraction.

**Statistical analysis:** Log-rank Mantel-Cox tests were performed to calculate survival curves shown in figures 2G, 2H. Two-tailed Mann-Whitney tests were performed in figures 2E, S2A, S2B, S2C. Unpaired t-tests were performed in figures 5F, S2F, S3B, S6B, S6C, S8E, S9B, S9C, S9D, S11A, S11E, S11F. Multiple t-test analysis was performed for the experiments in figure 1E and S3D. Two-way ANOVA with Sidak's multiple comparisons test was performed in the experiments in figures 1C and 1F. Wilcoxon matched-pairs test was performed in the experiment in figure 2F.

All data quantification and the statistical analysis described above were performed using Prism (v8).

**Data availability**

The datasets generated and analyzed during the current study are available in the GEO repository, code GSE148313 and can be found at https://www.ncbi.nlm.nih.gov/geo/query/acc.cgi?acc=GSE148313

# 3. Results

## *3.1 Nuclear FGFR1 promotes antiestrogen resistance*

We performed immunohistochemistry (IHC) and fluorescent in situ hybridization (FISH) of FGFR1 in 155 biopsies from women with operable ER+ breast cancer who received letrozole for 10-21 days before surgery (in trial NCT00651976) (Figure S1A) (12,24). In this published trial, response to estrogen suppression with letrozole was defined on the basis of post-treatment Ki67 levels [sensitive: natural log (ln) of post-letrozole Ki67 ≤1.0 or ≤2.4% tumor cells; intermediate: ln=1.1–1.9 or 2.5–7.3% tumor cells; resistant: (ln ≥2.0 or ≥7.4% tumor cells)]. Nineteen (19/155, 12%) tumors exhibited FGFR1 amplification, defined as an *FGFR1:CEN8* ratio ≥2.0 (Figure S1B). IHC revealed that, in addition to faint FGFR1 cytosolic staining, FGFR1 was clearly localized in breast cancer cell nuclei (Figure 1A). We observed similar FGFR1 localization in three ER+/*FGFR1*-amplified PDXs (Figures S1C, D). Subcellular fractionation of the PDX lysates revealed that, in addition to the expected localization in the plasma membrane, a substantial fraction of FGFR1 was detected in nuclear fractions (Figure S1E). ER+/*FGFR1*-amplified CAMA1 and MDA-MB-134 human breast cancer cell fractions also showed nuclear and chromatin-bound FGFR1 (Figure S1F).

We next correlated FGFR1 localization with response to estrogen suppression. Nuclear FGFR1 levels in these tumors positively correlated with post-letrozole Ki67 values (Figure 1B, $p$=0.034 and S2A, $p$=0.0055). Although nuclear FGFR1 levels tended to be higher in *FGFR1*-amplified compared to non *FGFR1*-amplified tumors, this difference was not statistically significant (Figure S2B, $p$=0.096). Further, analysis of only those tumors without *FGFR1*-amplification (n=136) revealed that high nuclear FGFR1 correlated with higher on-treatment Ki67 (Figure S2C, $p$=0.027), suggesting that nuclear FGFR1 protein levels are associated with antiestrogens resistance regardless of *FGFR1* gene copy number.

Next, to explore a causal association of nuclear FGFR1 with antiestrogen resistance, we transduced MCF-7 cells with an FGFR1(SP-)(NLS) plasmid (33) (Figure S2D). The lack of an N-terminal Signal Peptide (SP-) sequence and the presence of a strong Nuclear Localization Signal

(NLS) (PKKKRKV) are intended to prevent membrane localization of the resulting protein, while enforcing its nuclear localization. Indeed, the levels of FGFR1 in the nucleus of MCF-7 cells were increased upon transfection with FGFR1(SP-)(NLS), as shown by subcellular fractionation assay (Figure S2E) and immunofluorescence analysis (Figure S2F). MCF7$^{FGFR1(SP-)(NLS)}$ cells exhibited higher estrogen-independent growth (Figure 1C) and reduced sensitivity to fulvestrant (Figure 1D, E) compared to control cells. We next implanted MCF7$^{EV}$ and MCF7$^{FGFR1(SP-)(NLS)}$ cells in ovariectomized athymic mice. In agreement with the *in vitro* findings, MCF7$^{FGFR1(SP-)(NLS)}$ xenografts exhibited higher estrogen-independent growth compared to control tumors (Figure 1F). Further, while fulvestrant treatment induced tumor regression in control tumors, MCF7$^{FGFR1(SP-)(NLS)}$ xenografts did not regress (Figure 1F). Gene Set Enrichment Analysis (GSEA) of the 3,014 differentially expressed genes (DEGs) in MCF7$^{FGFR1(SP-)(NLS)}$ vs MCF7$^{EV}$ cells (shown in figure S2G) also revealed enrichment of gene sets associated with resistance to endocrine therapy and to tamoxifen (Figure 1G), suggesting that nuclear FGFR1 overexpression induces a transcriptional profile causal to antiestrogen resistance in breast cancer. Finally, we observed that both overexpression of FGFR1 wild-type and FGFR1(SP-)(NLS) in MCF7 cells resulted in enhanced estradiol-independent growth and reduced sensitivity to fulvestrant and tamoxifen (Figures S3A-E).

## *3.2 Nuclear FGFR1 occupies chromatin at transcription start sites of genes associated with antiestrogen resistance*

We next examined a role of nuclear FGFR1 in transcriptional regulation in breast cancer. To study chromatin occupancy by FGFR1, we performed ChIP-Seq in CAMA1 cells cultured for 48 h in estradiol-deprived media, which identified 4412 high-confidence binding sites. (Figure 2A). *De novo* consensus motif discovery analysis of the FGFR1 DNA-binding sites revealed GC-rich motifs among the top enriched motifs (Figures 2B and S4A).

Most mammalian promoters (i.e., regions upstream the transcription start sites) are enriched with GC-rich sequences, also named CpG islands (CGIs) (34,35). Also, many human active promoters are enriched with SP1, Nrf-1, E2F and ETS transcription factor-binding sites motifs, all containing

CGIs (36,37). Consistent with the predominance of GC-rich motifs identified (Figures 2B and S4A), the majority of FGFR1 binding sites were near the transcription start site (TSS) (Figure 2C), with 67% of ChIP-Seq peaks occurring at gene promoters (Figure 2D). Based on the nucleotide sequence of FGFR1-bound genomic loci identified by ChIP-Seq (Figure S5A), we next designed specific primer pair sequences to validate FGFR1 occupancy at nine selected promoter regions in CAMA1 (Figure S5B) and MDA-MB-134 cells (Figure S5C) by ChIP-qPCR. We further examined the binding of FGFR1 to the same promoter regions in tumor epithelial cells isolated by FACS from disaggregated HCI-011 PDXs (Figure S5D). For this, we performed ChIP-qPCR on the isolated tumor epithelial cells and confirmed enrichment of FGFR1 at similar promoter regions examined in CAMA1 and MDA-MB-134 cells (Figure S5E). These results suggest that FGFR1 binds to gene promoters and support a role for FGFR1 in transcriptional regulation.

RNA-Seq analysis of CAMA1 cells cultured for 48 h in estrogen-deprived media revealed that the average expression of genes whose promoter was bound by FGFR1 was significantly higher than the expression of all other genes (Figure 2E; Mann-Whitney, $p<0.0001$), implying that FGFR1 target genes are actively transcribed. Silencing of FGFR1 with siRNA significantly reduced the expression of genes whose promoters is bound by FGFR1 (Figure 2F, Wilcoxon test $p<0.0001$).

We intersected the list of 2901 genes whose promoter was bound by FGFR1, as identified by ChIP-Seq, with the 2048 genes downregulated by FGFR1 siRNA in CAMA1 cells (Figure S6A). A polygenic risk score was generated based on the 561 overlapping genes (Figure S6A). Analysis of 212 ER+/HER2- primary breast tumors in TCGA with known 8p11.23 copy number, where the FGFR1 locus lies, showed that the signature score was enriched in cancers with 8p11.23 amplification, compared to all other samples not harboring 8p11.23 copy gain or amplification (Figure S6B; t-test, $p=0.039$). In the METABRIC cohort of 1,294 ER+/HER2- breast cancers, the signature score was enriched in tumors exhibiting 8p11.23 amplification, compared to cancers without FGFR1 copy gain or amplification (Figure S6C; t-test, $p=0.038$). These results suggest that FGFR1-induced transcriptional signature is statistically enriched in primary breast tumors harboring *FGFR1* gene amplification. We next investigated whether the FGFR1-associated risk score correlated with antiestrogen resistance. In the METABRIC cohort of ER+ breast cancers

treated with antiestrogens (n=950), the risk score correlated with a worse DFS (Figure 2G; Log rank *p*=0.0103, HR=1.57, 95% CI 1.12 – 2.21, median 278.4 vs not reached) and OS (Figure 2H; Log rank *p*<0.0001, HR=1.72, 95% CI 1.35 – 2.18, median 126.5 vs 188.2 months). Taken together, these findings further suggest a role for nuclear FGFR1 in resistance to endocrine therapy.

### *3.3 FGFR1 associates with RNA Polymerase II and promotes gene expression*

To further dissect the function of FGFR1 in transcriptional regulation, we sought to uncover which components of the transcriptional machinery physically interact with nuclear FGFR1. For this purpose, we transduced CAMA1 cells with an FGFR1-3XFLAG lentiviral vector. Next we immunoprecipitated FLAG from mixed nuclear and chromatin fractions of CAMA1$^{FGFR1\text{-}3XFLAG}$ cells followed by mass spectrometry (MS) of the antibody pulldowns. Among the proteins recovered in the nuclear FGFR1 interactome, we found several RNA Polymerase II (Pol II) subunits (Figure 3A, B). RNA Pol II plays a pivotal role in gene transcription, that also requires other proteins critical for RNA polymerase recruitment to promoters, transcriptional initiation, and elongation (38). These findings were in line with enrichment of FGFR1 binding near transcription start sites (shown in Figure 2C), which are also the sites where Pol II is recruited for transcription initiation. We confirmed the FGFR1-Pol II association by co-precipitation with an FGFR1 antibody followed by Pol II western blot analysis of CAMA1 and MDA-MB-134 cell lysates (Figures 3C and S7A) and of HCI-011 PDX lysates (Figure S7B). FGFR1-Pol II co-precipitation was observed when we performed sonication and nuclease treatment, allowing the release of more soluble Pol II.

FGFR1 interacted with Pol II phosphorylated on Ser5 and Ser2 of the C-terminal domain (CTD) of the largest Pol II subunit, RPB1 (Pol II S5P, Pol II S2P) (Figures 3C, S7A-C). Phosphorylation of Ser5 and Ser2 on the CTD are post-translational modifications required for transcription initiation and elongation, respectively (39,40). MS analysis of CAMA1$^{FGFR1\text{-}3XFLAG}$ pulldowns also revealed proteins known to be directly involved in Pol II phosphorylation and subsequent transcriptional activity, such as CDK7 and CDK9 (41). We next confirmed the association of

FGFR1 with CDK7-CDK9 in CAMA1 and MDA-MB-134 cells by co-precipitation with an FGFR1 antibody (Figure S7D). The binding of FGFR1 with Pol II S5P, Pol II S2P, CDK7 and CDK9 was also confirmed by immunoprecipitation assays with Pol II S5P, Pol II S2P, CDK7 and CDK9 antibodies, followed by western blot analysis for FGFR1, in CAMA1 cells (Figure S7E). Comparison of the genomic coordinates of FGFR1 occupancy with data from previously published ChIP-Seq datasets for transcription factors (42) identified RNA Polymerase II subunit B1, RPB1 (*POLR2A*), as one of the top hits (Figure S8A). Using ChIP-Seq to evaluate the distribution of Pol II S5P across the CAMA1 cells genome, we found that 2867/4412 (65%) FGFR1 binding peaks overlapped with Pol II S5P binding sites (Figures 3D, E), with distribution around similar locations near the TSS (Figures 3F, 3G and S8B), further suggesting that FGFR1 genomic distribution occurs at actively transcribed loci. ChIP-reChIP assays, with sequential FGFR1 and Pol II S5P antibodies, confirmed FGFR1-Pol II S5P association at selected gene promoters in CAMA1 (Figures 3H and S8C) and MDA-MB-134 cells (Figure S8D). Finally, by RT-qPCR we confirmed that silencing FGFR1 by siRNA in CAMA1 cells resulted in downregulation of selected FGFR1 target genes (Figure S8E). Taken together, these findings suggest that FGFR1 is part of a chromatin-associated Pol II complex engaged in active transcription.

Using MCF7$^{FGFR1(SP-)(NLS)}$ cells, we next investigated the effect of exogenous nuclear FGFR1 in gene transcription. By ChIP-Seq, we identified 24,475 FGFR1 DNA binding sites in MCF7$^{FGFR1(SP-)(NLS)}$ cells, corresponding to 11,840 genes (Figure 3I). We intersected the FGFR1-bound genes with the differentially regulated transcripts (FDR<0.05) in MCF7$^{FGFR1(SP-)(NLS)}$ vs MCF7$^{EV}$ cells (shown in Figure S2G), finding that 1,009 of the 1,454 upregulated genes and 1,141 of the 1,560 downregulated genes were also bound by FGFR1 at a genomic level (Figure 3I). To examine whether nuclear FGFR1 directly affects gene expression in MCF7$^{FGFR1(SP-)(NLS)}$ cells, we used Binding and Expression Target Analysis (BETA) platform, a computational program which integrates ChIP-Seq and RNA-Seq data (43). Results from this analysis suggested a direct role for genomic-bound FGFR1 in activating gene expression ($p$=8.01e-06; Figure 3J). Conversely, there was no significant association between FGFR1-bound loci and repressed genes ($p$=0.139; Figure 3J). GSEA of the 1,009 genes upregulated in MCF7$^{FGFR1(SP-)(NLS)}$ and bound by FGFR1 at

a genomic level (shown in Figure 3I) revealed a strong enrichment of estrogen response early (FDR = 2.29e-44) and late (FDR = 6.43e-33) genes (Figure S9A), suggesting that nuclear FGFR1 induces an ERα-associated transcriptional profile that may contribute to endocrine resistance. By RT-qPCR, we confirmed the upregulation of canonical ERα-regulated genes in MCF7$^{FGFR1(SP-)(NLS)}$ cells compared to control cells (Figure S9B). We hypothesized that FGFR1 may regulate the expression of canonical ERα-regulated genes independent of ERα transcription. To support this, we performed RT-qPCR analysis of xenografts treated with fulvestrant (Figure 1F). In both MCF7$^{EV}$ and MCF7$^{FGFR1(SP-)(NLS)}$ xenografts, fulvestrant treatment suppressed ERα protein expression by IHC (Figure S9C). Expression of canonical ERα target genes was downregulated in fulvestrant-treated MCF7$^{EV}$ xenografts but not in fulvestrant-treated MCF7$^{FGFR1(SP-)(NLS)}$ xenografts (Figure S9D), suggesting that nuclear FGFR1 induces the expression of an ERα-associated signature independent of ERα transcription.

### *3.4 Nuclear FGFR1 overlaps with active transcription histone marks*

To examine if FGFR1 is associated with active gene transcription, we first superimposed the genomic coordinates of FGFR1-binding sites in CAMA1 cells with those from publicly available ChIP-Seq datasets for histone marks (42). This analysis revealed a strong enrichment for active transcription histone marks, such as H3K4me3 and H3K27ac (Figure S10A). H3K4me3 is commonly enriched around TSS of actively transcribed genes (44). Similarly, H3K27 acetylation is a marker of active regulatory elements and found at both promoters and enhancers (45). We next analyzed the genomic distribution of H3K27ac in CAMA1 cells by ChIP-Seq. Notably, 3961/4175 (94.8%) of FGFR1 peaks overlapped with H3K27ac, suggesting that FGFR1 binding to DNA occurs at genomic loci that are enriched for promoters of actively transcribed genes (Figures 4A, B). We also investigated the distribution of the H3K4me3 histone mark in CAMA1 cells. In agreement with the finding of FGFR1 enrichment at TSSs/promoter regions (shown in Figures 2C, D), we identified a strong overlap between FGFR1 and H3K4me3 (4055/4265 sites or 95%), implying that FGFR1 is occupying sites engaged in transcription initiation (Figures 4C, D). Taken together, our findings suggest that FGFR1 is recruited to genomic regions where

epigenetic modifications, such as H3K27 acetylation and H3K4 trimethylation, co-occur in order to promote a chromatin state accessible for active transcription complexes at promoter regions (Figure 4E).

### *3.5 FOXA1 mediates FGFR1 recruitment to chromatin*

We next sought to identify mechanisms regulating FGFR1 recruitment to chromatin. To this end, we further examined the list of FGFR1-interacting proteins identified by MS of FLAG antibody pulldowns from mixed nuclear and chromatin bound CAMA1$^{3XFLAG\text{-}FGFR1}$ cell fractions. Our attention was captured by FOXA1 (Forkhead Box A1) (Figure 5A), a master regulator that modifies chromatin accessibility for transcription factors (46). FOXA1 has been shown to be required for estrogen receptor binding to chromatin and to induce antiestrogen resistance in ER+ breast cancer (47,48). FOXA1 also influences the genomic binding of other transcription factors, such as the androgen receptor in prostate cancer, contributing to castration resistance in these tumors (49). FOXA1 is required for the survival of ER+ breast cancer cells, as demonstrated by Dependency Map Project (https://depmap.org/portal/) (50) (Figure S11A), and has the ability to promote the association of transcription factors with chromatin (51). Thus, we sought to determine whether FOXA1 affects FGFR1 transcriptional function.

Co-immunoprecipitation of CAMA1 and MDA-134 cell lysates with an FGFR1 antibody followed by FOXA1 western showed association of FOXA1 with FGFR1 (Figures 5B and S11B). We next investigated the FOXA1 genomic distribution in CAMA1 cells by ChIP-Seq. We found that 1,669/4,438 (38%) of FGFR1 DNA binding sites were shared with FOXA1 (Figures 5C and S11C). ChIP-reChIP experiments, conducted by sequential chromatin immunoprecipitation of FGFR1 and FOXA1, confirmed that these two proteins are both present in the transcriptional complex binding at selected genomic loci in CAMA1 and MDA-MB-134 cells (Figures 5D and S11D). Finally, we silenced FOXA1 in CAMA1 cells using siRNA. Notably, 52% of FGFR1 binding peaks were reduced or lost upon FOXA1 suppression (Figure 5E). Using ChIP-qPCR, we confirmed that FGFR1 recruitment to target genomic loci was significantly reduced upon FOXA1 knockdown in CAMA1 and MDA-MB-134 cells (Figures 5F and S11E). Expression of FGFR1 target genes was

reduced by siFOXA1 as measured by RT-qPCR (Figure S11F). Of note, FOXA1 knockdown did not have any effect on FGFR1 expression or protein levels (Figure S11G). Altogether, these data suggest a role for FOXA1 in regulating FGFR1 recruitment to chromatin and, consequently, its transcriptional activity.

### *3.6 Nuclear FGFR1 activity is enhanced by FGF2 but not affected by receptor tyrosine kinase blockade*

Previous studies have shown that growth factors such as EGF and insulin can induce nuclear trafficking of EGFR and Insulin Receptor (IR), respectively, enhancing their transcriptional activity (19,21). FGF2 and FGFR1 have been shown to co-localize in the nucleus of pancreatic cancer cells, promoting an invasive phenotype (14). In contrast to FGFR1, FGF2 contains an NLS peptide sequence, which may promote importin β-mediated translocation of FGFR1 into the nucleus (52). Thus, we examined if growth factor stimulation influences FGFR1 transcriptional function in breast cancer cells. Stimulation with FGF2 increased FGFR1 levels in subcellular nuclear fractions of CAMA1 cells (Figure S12A) as well as the FGFR1-Pol II S5P association measured by co-immunoprecipitation followed by immunoblot analysis (Figure S12B). To further characterize the effect of FGF2 on FGFR1-mediated transcription, we first performed RNA-Seq analysis of FGF2-stimulated CAMA1 cells. This analysis identified 7,923 differentially expressed (DEGs) as a function of FGF2 treatment (FDR <0.05) (Figure 6A). Integration of the RNA-Seq data and FGFR1 ChIP-Seq results from FGF2-stimulated CAMA1 cells (shown in figure S12C) with the BETA platform (43) suggested that FGFR1 DNA binding sites have a significant role in promoting FGF2-induced transcription (Figure 6B, $p$=0.029). Conversely, there was not a statistical association between FGFR1 DNA binding sites and FGF2-repressed genes ($p$=0.392). We also employed the Genomic Regions Enrichment of Annotations Tool (GREAT) (53) to interpret the biological functions of FGFR1 DNA binding sites identified by ChIP-Seq in FGF2-treated CAMA1 cells. Consistent with the BETA platform, genes associated with FGFR1 DNA binding sites were highly enriched for signatures of cellular response to growth factor stimulation and activation of the FGFR pathway (Figure 6C).

The effects of FGF2 on nuclear translocation and transcriptional regulation suggested a causal link with the FGFR1 tyrosine kinase activity. Thus, we investigated the effect of the pan-FGFR tyrosine kinase inhibitor (TKI) erdafitinib (54). Treatment with erdafitinib abolished FGFR1, FRS2$\alpha$ and ERK phosphorylation/activation (Figure S12D) but did not abrogate the FGF2-induced increase in FGFR1 levels in CAMA1 cell nuclear fractions (Figure 6D). Further, treatment with erdafitinib did not affect the FGF2-induced association of FGFR1 with Pol II S5P association (Figure 6E) nor the FGFR1 genomic distribution as shown by ChIP-Seq of CAMA1 cells (Figures 6F and S12E). Finally, treatment with erdafitinib did not impair growth of MCF7$^{FGFR1(SP-)(NLS)}$ cells, compared to MCF7$^{EV}$ cells (Figure S12F), suggesting the FGFR1 activated TK is not causally associated with the receptor's activity in the nucleus.

# 4. Discussion

FGFR signaling has multifaceted roles in normal physiology and development, such as embryogenesis, organ development, tissue repair, remodeling, angiogenesis and metabolism (55-58). Gene rearrangements, activating tyrosine kinase domain mutations, and fusions in FGFR genes are oncogenic drivers in several cancer types, such as breast, bladder, and biliary duct tumors (59-61). The canonical FGFR pathway is triggered by activation of the receptor's tyrosine kinase at the plasma membrane followed by induction of signaling nodes, primarily RAS/RAF/MEK/ERK and PI3K/AKT. However, recent work has shown the presence of FGFR receptors, such as FGFR2, in the nucleus of cancer cells where it may affect gene transcription (62). In medulloblastoma cells, nuclear FGFR1 has been shown to bind CREB-Binding Protein (CBP) and modulate its transcriptional activity (17). We found FGFR1 abundance in the nucleus of breast cancer cells in ER+ primary tumors and PDXs (Figures 1A, S1C and S1E). Therefore, we investigated herein the role of nuclear FGFR1, which may shed light on mechanisms by which aberrant FGFR signaling drives cancer progression and its therapeutic implications.

FGFR1 overexpression has been shown to induce antiestrogen resistance (12,22,23). In line with these reports, we found that high nuclear levels of FGFR1 are associated with a lower response to estrogen suppression in ER+ tumors in patients (Figures 1B and S2A). This correlation between nuclear FGFR1 levels and resistance to estrogen suppression was independent of *FGFR1* gene amplification (Figure S2C). Accordingly, MCF7 cells transduced with an FGFR1 expression vector containing a strong nuclear localization sequence exhibited robust growth in the absence of estrogen and, when established as xenografts in ovariectomized mice, were relative resistant to the ER antagonist fulvestrant (Figures 1C-F). In these cells, genomic-bound FGFR1 induced the expression of estrogen receptor early and late genes sets (Figure S9A), suggesting that nuclear FGFR1 contributes to endocrine resistance promoting the ERα-associated transcriptional profile. Further, a gene signature score based on the gene promoters bound by FGFR1 using an approach previously used to predict genes near ERα binding sites in breast cancer (63), was associated with antiestrogen resistance in the METABRIC cohort of

patients with ER+ breast cancer treated with antiestrogens (Figures 2G, H). Further suggesting a clinical significance of our findings, the FGFR1-induced polygenic risk score also correlated with FGFR1 copy number alterations in two large datasets of patients, TCGA and METABRIC (Figures S6B, C).

Mapping of FGFR1 genomic occupancy in ER+/*FGFR1*-amplified breast cancer cells by ChIP-Seq revealed marked enrichment at TSS/promoter regions (Figures 2C, D). Supporting a role of FGFR1 recruitment in active gene transcription, FGFR1 coupled with phosphorylated RNA-Polymerase II (Figures 3C, S7A-C). This hypothesis was further strengthened by the overlap of FGFR1 with histone marks H3K27ac and H3K4me3 (Figures 4A, C), representative of promoters of actively transcribed genes. These findings are in line with previous studies reporting FGFR1 localization to nuclear speckles, which are sites of active transcription, and colocalization with RNA Pol II in TE671 human medulloblastoma cells (64). To the best of our knowledge, this is the first report describing the genome-wide distribution of FGFR1 in cancer.

The interaction of FGFR1 with CDK7, CDK9, Cyclin H, CTR9, and MED family proteins, revealed by MS (Figure S7D), further supported the notion that FGFR1 is part of a complex that regulates gene transcription. FGFR1 does not harbor a *bona fide* DNA binding domain. Thus, it is likely that FGFR1 is tethered to promoters through interaction with other proteins, presumably general transcription factors. We also showed that FOXA1 plays a significant role in the recruitment of FGFR1 to chromatin. FOXA1 orchestrates transcription factor binding to chromatin and drives gene expression that results in endocrine therapy resistance in cancer (65,66). FOXA1 pioneering function has been shown to be independent on steroids and hormone signaling (51) but can be affected by mitogenic signals (63). Also, since FOXA1 is currently considered undruggable, understanding how extracellular and intracellular signals modulate FOXA1-FGFR1 interaction may provide rationale to test new therapeutic strategies to inhibit FGFR1 transcriptional function.

Our findings provide new insight into the biology and oncogenic functions of RTKs. For example, nuclear EGFR has been associated with resistance to the anti-EGFR antibody cetuximab (67). EGFR nuclear translocation has been associated with resistance to chemotherapy and ionizing

radiation in lung cancer cells, primarily by modulating the DNA repair process (68). Nuclear HER2 was reported to be involved in resistance to the HER2 antibody trastuzumab in HER2+ breast cancer cells (69). More recently, Hancock *et al.* reported an unexpected role of the nuclear insulin receptor (INSR) as a transcription factor that induces gene expression associated with insulin-related functions and insulin resistance (19). Previous studies showed that ligand activation of membrane-bound FGFR1 can induce its migration to the nucleus, mainly by importin β family proteins (14,52). There is also evidence that Sec61 α family proteins can mediate translocation of newly synthesized FGFR1 from the endoplasmic reticulum to the nucleus (70). A complete understanding of the factors regulating these mechanisms could identify new therapeutic targets in order to suppress FGFR1 nuclear localization and FGFR1-induced gene expression.

FGFR TKIs have been clinically effective against cancers harboring FGFR alterations acting as dominant oncogenic drivers, such as FGFR3 mutations or fusions in urothelial carcinoma, or FGFR2 fusions in cholangiocarcinoma (71,72). Even though testing has been more limited in patients with *FGFR1*-amplified breast cancer, FGFR TKIs have not shown any meaningful clinical activity against these tumors (73,74). The reasons for this failure may be attributed to various reasons. First, the inhibitors that have been tested are not specific and exhibit non-FGFR associated toxicities that limit their dosing (1). Second, it is not clear to what extent *FGFR1*-amplified tumors depend on canonical FGFR signaling. Third, there is not agreement regarding the optimal threshold of copy number to be used to stratify patients enrolled in clinical trials. Results from the study showed herein may shed light on an unconventional role of FGFR1 in these tumors, different from the classical RTK-induced signaling and, as such, have translational implications for drug development. For example, treatment with erdafitinib, a pan-FGFR TKI currently in clinical trials in breast cancer, did not affect nuclear FGFR1 levels and its genomic distribution (Figures 6D, F), nor growth of cells overexpressing nuclear FGFR1 (Figure S12F), ultimately suggesting that FGFR1 transcriptional activity is not influenced by therapeutic inhibition of the FGFR1 tyrosine kinase. We speculate this could explain at least in part the low activity of FGFR TKIs against FGFR1 overexpressing tumors. Taken together, these data provide a

rationale for the development of targeted therapies that inhibit nuclear FGFR1 function in ER+ breast cancer.

# 5. Acknowledgements

We thank the assistance of the UTSW Proteomics Core. We acknowledge Professor Yonghao Yu (Department of Biochemistry at UT Southwestern Medical Center) for sharing the pCDNA5-zz-FLAG plasmid. We thank Professor Michal Stachowiak (State University of New York) for sharing the pCDNA3.1(-)FGFR1(SP-)(NLS) plasmid. We thank Professor Alana Welm (University of Utah) for sharing the HCI-003 and HCI-011 PDXs.

**Financial support**: UTSW Simmons Cancer Center P30 CA142543, CPRIT RR170061, NCI Breast SPORE P50 CA098131, Vanderbilt-Ingram Cancer Center P30 CA68485, Susan G. Komen Breast Cancer Foundation SAC100013, Breast Cancer Research Foundation, NCI R01CA224899 , Susan G. Komen Postdoctoral Fellowship PDF17487926, Associazione Italiana per la Ricerca sul Cancro (AIRC) Investigator Grant IG2018-21339 and AIRC My First Grant MFGA2018-21505.

# 6. Figures

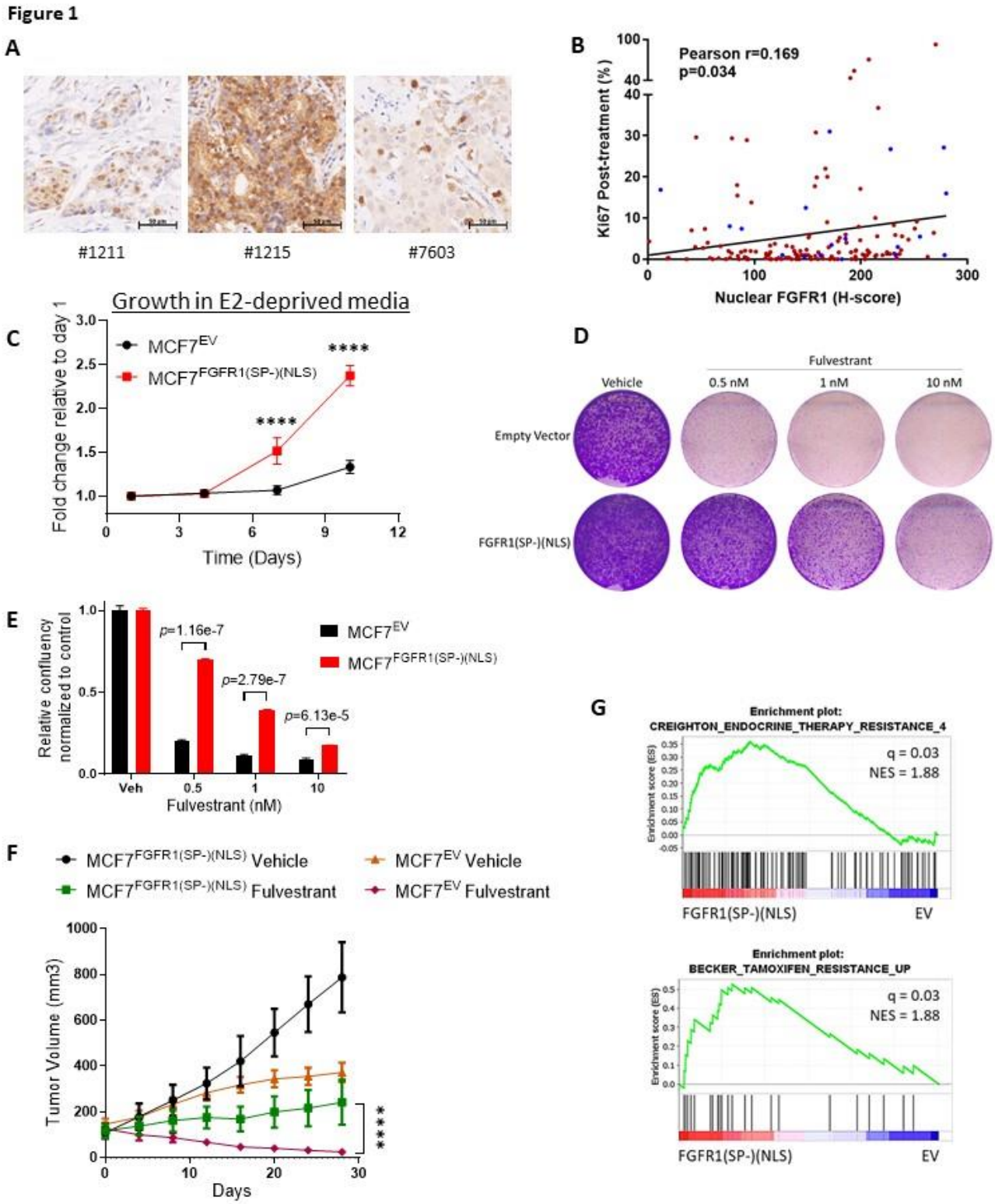
Figure 1
A
#1211
#1215
#7603
B
Pearson r=0.169
p=0.034
KI67 Post-treatment (%)
Nuclear FGFR1 (H-score)
C
Growth in E2-deprived media
MCF7EV
MCF7FGFR1(SP-)(NLS)
****
****
Fold change relative to day 1
Time (Days)
D
Fulvestrant
Vehicle
0.5 nM
1 nM
10 nM
Empty Vector
FGFR1(SP-)(NLS)
E
p=1.16e-7
p=2.79e-7
p=6.13e-5
MCF7EV
MCF7FGFR1(SP-)(NLS)
Relative confluency normalized to control
Veh
0.5
1
10
Fulvestrant (nM)
F
MCF7FGFR1(SP-)(NLS) Vehicle
MCF7FGFR1(SP-)(NLS) Fulvestrant
MCF7EV Vehicle
MCF7EV Fulvestrant
Tumor Volume (mm3)
Days
****
G
Enrichment plot:
CREIGHTON_ENDOCRINE_THERAPY_RESISTANCE_4
q = 0.03
NES = 1.88
Enrichment score (ES)
FGFR1(SP-)(NLS)
EV
Enrichment plot:
BECKER_TAMOXIFEN_RESISTANCE_UP
q = 0.03
NES = 1.88
Enrichment score (ES)
FGFR1(SP-)(NLS)
EV

**Figure 1. Nuclear FGFR1 promotes antiestrogen resistance.** (A) Sections of FFPE of ER+/*FGFR1*-amplified breast primary tumors were subjected to IHC with an FGFR1 antibody as described in the methods. (B) Plot showing direct correlation between nuclear FGFR1 H-Score, measured by IHC, and post-treatment Ki67 in 155 ER+/HER2- breast cancer biopsies from women treated with pre-operative letrozole for 10-21 days in the NCT00651976 trial (12,24). In blue, samples exhibiting *FGFR1* amplification (n=19/155), defined as an *FGFR1:CEN8* ratio ≥2.0. (C) MCF-7$^{EV}$ and MCF-7$^{FGFR1(SP-)(NLS)}$ cells were seeded in 6-well plates in estrogen-deprived media. Media was replenished every 72 hours. Monolayers were stained with crystal violet on days 1, 4, 7 and 10. Quantification of the integrated intensity values as fold change normalized to day 1 (Sidak's multiple comparisons test, two-way ANOVA, **** $p$<0.0001). (D) MCF-7$^{EV}$ and MCF-7$^{FGFR1(SP-)(NLS)}$ cells were seeded in 6-well plates in full media and treated with vehicle (DMSO) or fulvestrant. After seven days, monolayers were stained with crystal violet. (E) Quantification of the integrated intensity values as fold change normalized to vehicle-treated controls (Multiple Student's t-test). (F) MCF-7$^{EV}$ and MCF-7$^{FGFR1(SP-)(NSL)}$ xenografts were established in ovariectomized athymic mice implanted with a s.c. 14-day release, 0.17-mg 17β-estradiol pellet. Once tumors established, mice were randomized to treatment with vehicle or fulvestrant (5 mg/week). Each data point represents the mean tumor volume in mm$^3$ ± SEM (n=8 per arm, ****$p$ < 0.0001; Two-way ANOVA). (G) GSEA of RNA-Seq data for MCF7$^{FGFR1(SP-)(NLS)}$ versus MCF7$^{EV}$, showing enrichment of gene sets associated with antiestrogen resistance in MCF7$^{FGFR1(SP-)(NLS)}$ cells.

**Figure 2**

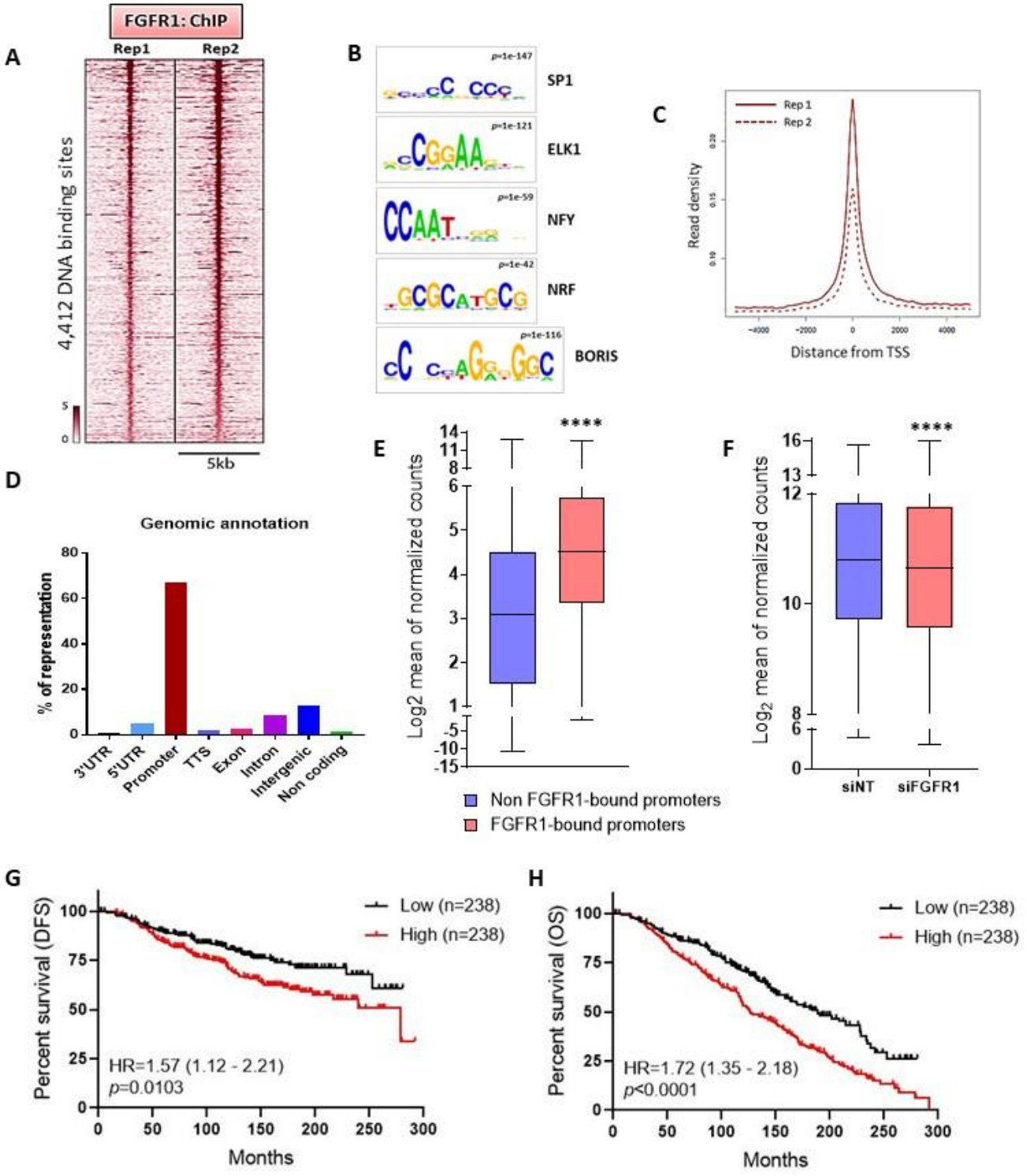
A
FGFR1: ChIP
Rep1
Rep2
4,412 DNA binding sites
5kb
B
SP1
ELK1
NFY
NRF
BORIS
C
Rep 1
Rep 2
Read density
Distance from TSS
D
Genomic annotation
% of representation
3'UTR
5'UTR
Promoter
TTS
Exon
Intron
Intergenic
Non coding
E
Log2 mean of normalized counts
****
Non FGFR1-bound promoters
FGFR1-bound promoters
F
Log2 mean of normalized counts
****
siNT
siFGFR1
G
Percent survival (DFS)
Low (n=238)
High (n=238)
HR=1.57 (1.12 - 2.21)
p=0.0103
Months
H
Percent survival (OS)
Low (n=238)
High (n=238)
HR=1.72 (1.35 - 2.18)
p<0.0001
Months

**Figure 2. Nuclear FGFR1 occupies chromatin at transcription start sites of genes associated with antiestrogen resistance.** (A) Heatmap showing ChIP-Seq read densities around the FGFR1 bound regions in CAMA1 cells, in two replicates. The x-axis represents read densities within 5-kb region around the peak summit; the y-axis represents each predicted binding site. Cells were cultured for 48 h in IMEM/10% CSS. (B) Top consensus motifs, identified by *de novo* motif analysis, at genomic loci bound by FGFR1 identified in A. Statistical significance expressed as *p* value for each motif is shown. (C) Plot representing the density of the FGFR1 distribution around the Transcription Start Sites (TSS) in the two ChIP-Seq replicates. (D) Genomic annotations for the FGFR1 binding sites identified by ChIP-Seq showing enrichment of promoter regions. (E) Expression level of genes whose promoter is bound by FGFR1 (red) (2704 genes) versus gene expression of all other genes (blue) (10,452 genes). Data are derived from RNA-Seq on CAMA1 cells cultured for 48 h in IMEM/10% CSS (**** $p<0.0001$, Mann-Whitney test). (F) Gene expression of genes whose promoter is bound by FGFR1 in CAMA1 cells upon siRNA-mediated FGFR1 knockdown (n=3) (**** $p<0.0001$, Two-tailed Wilcoxon test). (G) Disease Free Survival (DFS) and Overall Survival (H) of the METABRIC cohort of 950 ER+/HER2- breast cancer patients treated with antiestrogens as a function of the FGFR1-associated polygenic score (Lowest Quartile vs Highest Quartile). The signature score was calculated by GSVA (75).

**Figure 3**

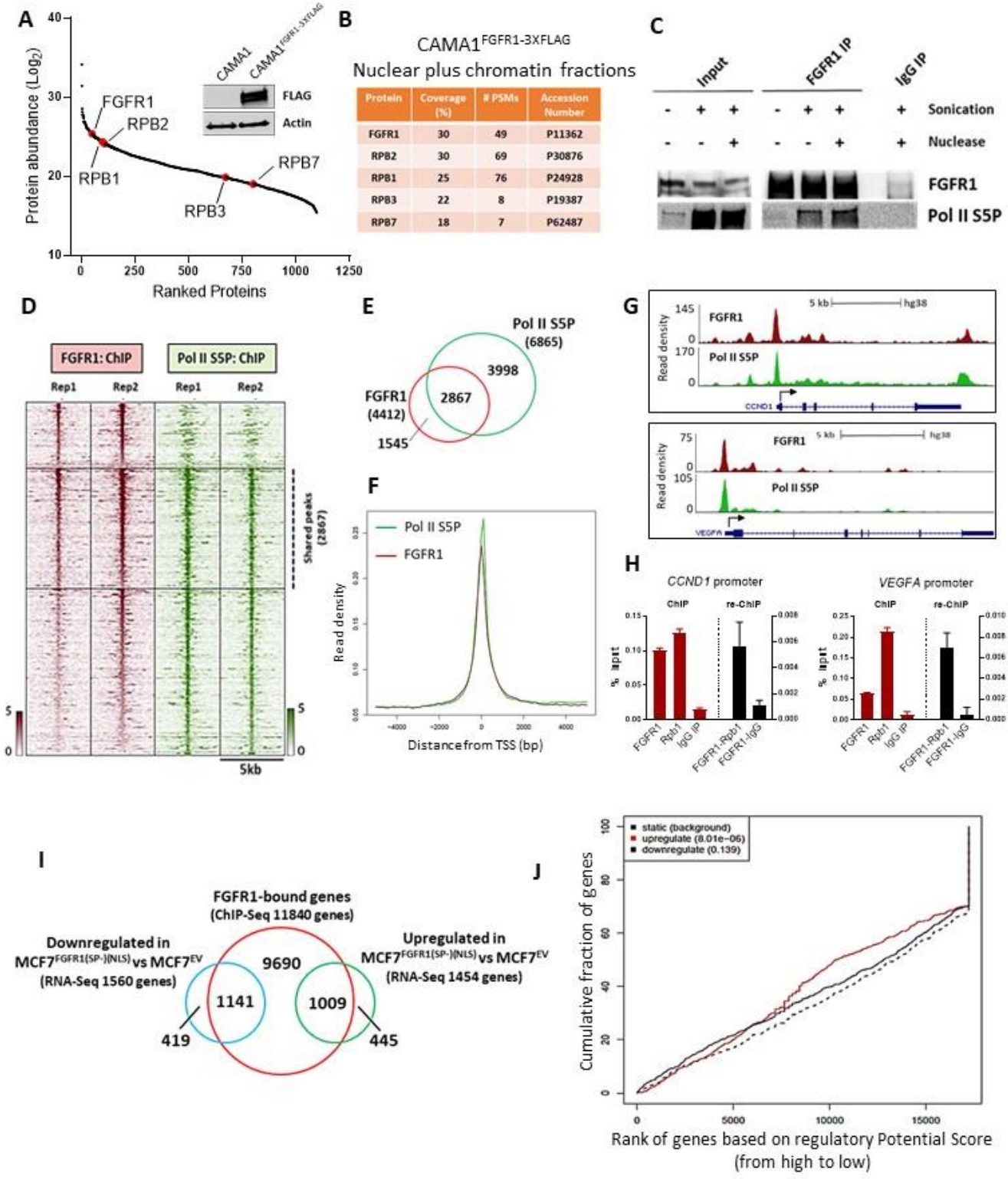
A
Protein abundance (Log2)
Ranked Proteins
FGFR1
RPB2
RPB1
RPB3
RPB7
CAMA1
CAMA1FGFR1-3XFLAG
FLAG
Actin
B
CAMA1FGFR1-3XFLAG
Nuclear plus chromatin fractions
Protein | Coverage (%) | # PSMs | Accession Number
FGFR1 | 30 | 49 | P11362
RPB2 | 30 | 69 | P30876
RPB1 | 25 | 76 | P24928
RPB3 | 22 | 8 | P19387
RPB7 | 18 | 7 | P62487
C
Input
FGFR1 IP
IgG IP
Sonication
Nuclease
FGFR1
Pol II S5P
D
FGFR1: ChIP
Pol II S5P: ChIP
Rep1
Rep2
Shared peaks (2867)
5kb
E
Pol II S5P (6865)
3998
FGFR1 (4412)
2867
1545
F
Pol II S5P
FGFR1
Read density
Distance from TSS (bp)
G
FGFR1
Pol II S5P
Read density
5 kb
hg38
CCND1
VEGFA
H
CCND1 promoter
VEGFA promoter
ChIP
re-ChIP
% Input
FGFR1
Rpb1
IgG IP
FGFR1-Rpb1
FGFR1-IgG
I
FGFR1-bound genes
(ChIP-Seq 11840 genes)
Downregulated in MCF7FGFR1(SP-)(NLS) vs MCF7EV
(RNA-Seq 1560 genes)
Upregulated in MCF7FGFR1(SP-)(NLS) vs MCF7EV
(RNA-Seq 1454 genes)
9690
1141
1009
419
445
J
static (background)
upregulate (8.01e-06)
downregulate (0.139)
Cumulative fraction of genes
Rank of genes based on regulatory Potential Score
(from high to low)

**Figure 3. FGFR1 associates with RNA Polymerase II and promotes gene expression.** (A) FLAG-immunoprecipitation followed by MS was performed on sonicated and nuclease-treated mixed nuclear and chromatin fractions of CAMA1$^{FGFR13XFLAG}$ cells. FGFR1 and RNA Polymerase II subunits are highlighted (red). The western blot on the right shows FLAG-FGFR1 overexpression in CAMA1$^{FGFR13XFLAG}$ cells. (B) List of RNA Polymerase II subunits that co-precipitate with FLAG-FGFR1. Coverage (%) indicates the percentage of the protein sequence that was covered by the identified peptides. #PSMs indicates the number of Peptide Spectrum Matches or the number of spectra assigned to peptides that contributed to inference of the protein. (C) Co-precipitation of FGFR1 and RNA Polymerase phosphorylated on Serine residue 5 (Pol II S5P), with or without sonication and nuclease treatment. (D) Heatmaps of ChIP-Seq read densities around the FGFR1 (red) and Pol II S5P bound regions (green) in CAMA1 cells. (E) Venn Diagram and (F) density plots related to FGFR1- and Pol II S5P-ChIP-Seq shown in D. (G) Distribution of FGFR1 and Pol II S5P binding peaks at the *VEGFA* and *CCND1* promoters (UCSC genome browser). (H) ChIP-reChIP assay performed by sequential ChIP-qPCR with a FGFR1 antibody followed by an antibody against Pol II S5P (Rpb1) or normal rabbit IgG (control), at the *VEGFA* and *CCND1* promoters. Enrichment values expressed as percent (%) of input. (I) Venn Diagram of FGFR1-bound genes by ChIP-Seq in MCF7$^{FGFR1(SP-)(NLS)}$ cells (red circle), and genes upregulated (green) and downregulated (blue) in MCF7$^{FGFR1(SP-)(NLS)}$ vs MCF7$^{EV}$ cells. (J) Prediction of activating or repressing transcription function of FGFR1 by Binding and Expression Target Analysis (BETA). ChIP-Seq and RNA-Seq data from I were integrated. Genomic regions bound by FGFR1 are predicted to regulate the expression of upregulated genes, but not of downregulated genes. *p* values indicate the significance of the associations compared to background non-regulated genes.

**Figure 4**

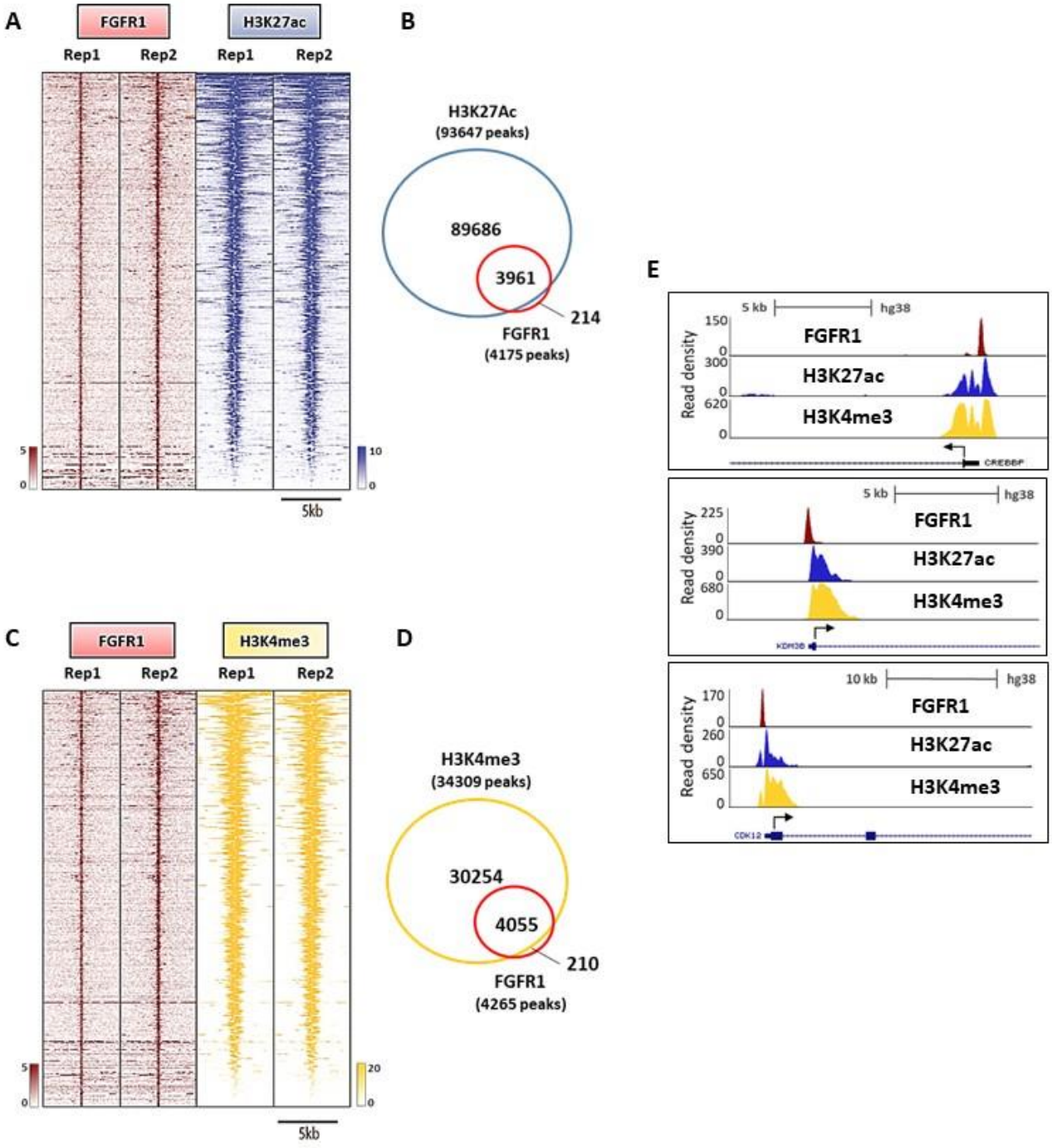
A
FGFR1
H3K27ac
Rep1
Rep2
Rep1
Rep2
5
0
10
0
5kb
B
H3K27Ac
(93647 peaks)
89686
3961
214
FGFR1
(4175 peaks)
C
FGFR1
H3K4me3
Rep1
Rep2
Rep1
Rep2
5
0
20
0
5kb
D
H3K4me3
(34309 peaks)
30254
4055
210
FGFR1
(4265 peaks)
E
5 kb
hg38
Read density
150
0
300
0
620
0
FGFR1
H3K27ac
H3K4me3
CREBBP
5 kb
hg38
Read density
225
0
390
0
680
0
FGFR1
H3K27ac
H3K4me3
KDM3B
10 kb
hg38
Read density
170
0
260
0
650
0
FGFR1
H3K27ac
H3K4me3
CDK12

**Figure 4. Nuclear FGFR1 overlaps with active transcription histone marks.** (A) Heatmaps of ChIP-Seq read densities around the FGFR1-bound regions (red) and areas of increased acetylation of H3K27 (H3K27ac, blue) in CAMA1 cells. Two replicates for each antibody are shown. (B) Venn diagram of FGFR1 ChIP-Seq peaks and H3K27ac regions. (C) Heatmaps of ChIP-Seq read densities around the FGFR1-bound regions (red) and areas of increased trimethylation of H3K4 (H3K4me3; yellow) in CAMA1 cells. Two replicates for each antibody are shown. (D) Venn diagram of FGFR1 ChIP-Seq peaks and H3K4me3 regions. (E) Distribution of FGFR1 binding peaks, H3K27ac and H3K4me3 histone marks at the *CREEBP, KDM4B* and *CDK12* promoters (UCSC genome browser)**.**

**Figure 5**

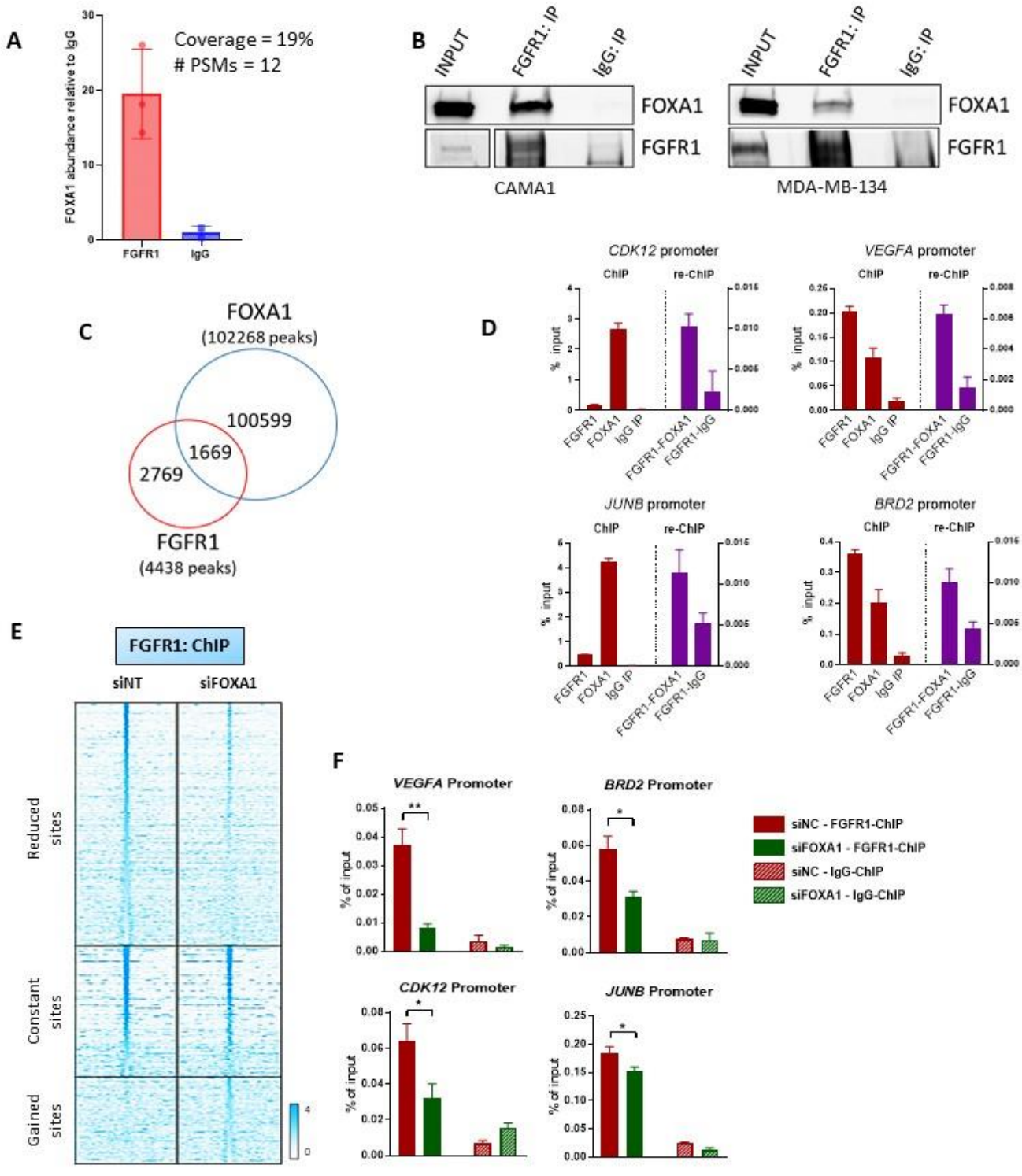
A
Coverage = 19%
# PSMs = 12
FOXA1 abundance relative to IgG
FGFR1
IgG
B
INPUT
FGFR1: IP
IgG: IP
FOXA1
FGFR1
CAMA1
MDA-MB-134
C
FOXA1
(102268 peaks)
100599
1669
2769
FGFR1
(4438 peaks)
D
CDK12 promoter
VEGFA promoter
JUNB promoter
BRD2 promoter
ChIP
re-ChIP
% input
FGFR1
FOXA1
IgG IP
FGFR1-FOXA1
FGFR1-IgG
E
FGFR1: ChIP
siNT
siFOXA1
Reduced sites
Constant sites
Gained sites
F
VEGFA Promoter
BRD2 Promoter
CDK12 Promoter
JUNB Promoter
% of input
siNC - FGFR1-ChIP
siFOXA1 - FGFR1-ChIP
siNC - IgG-ChIP
siFOXA1 - IgG-ChIP

**Figure 5. FOXA1 mediates FGFR1 recruitment to chromatin.** (A) Immunoprecipitation of FLAG-FGFR1 followed by mass spectrometry was conducted on mixed nuclear plus chromatin-bound fractions of CAMA1$^{3XFLAG\text{-}FGFR1}$ cells. The plot shows the enrichment of FOXA1 in the FLAG-FGFR1-bound fraction compared to IgG control. (B) Co-precipitation of FGFR1 and FOXA1, followed by western blot analysis, in CAMA1 (left panel) and MDA-MB-134 (right panel) cells. (C) Venn diagram of FGFR1 peaks (red circle), identified by ChIP-Seq (in Figure 2A) and FOXA1 DNA binding loci identified by ChIP-Seq (blue circle) in CAMA1 cells. (D) ChIP-reChIP assay performed by sequential ChIP-qPCR with a FGFR1 antibody followed by an antibody against FOXA1 or normal rabbit IgG, at the *BRD2, CDK12, VEGFA* and *JUNB* promoters. Enrichment values expressed as percent (%) of input. (E) Heatmaps of ChIP-Seq read densities around the FGFR1 bound regions in CAMA1 cells transfected with Non Targeting (siNT) or FOXA1 siRNAs. Twenty-four h post-transfection, dishes were replenished with IMEM/10% CSS and cells were collected 48 h later for CHIP. (F) ChIP-qPCR confirmation of reduced FGFR1 binding at selected genomic loci, *VEGFA* (t test, $p$=0.0071), *BRD2* ($p$=0.0145), *CDK12* ($p$=0.0114), *JUNB* ($p$=0.0252) promoters, upon siRNA-mediated FOXA1 knockdown in CAMA1 cells. Enrichment values expressed as percent (%) of input.

**Figure 6**

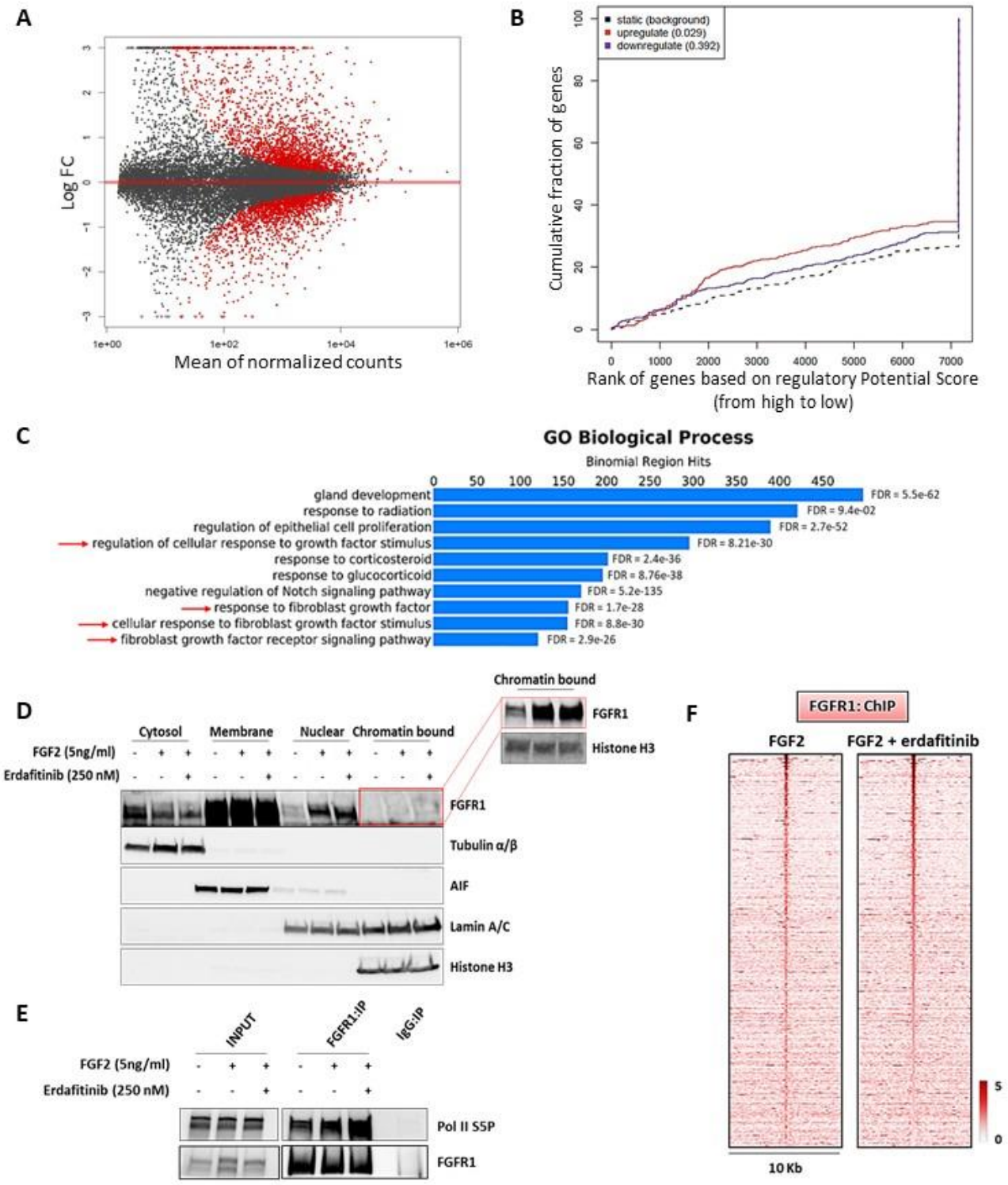
A
Log FC
Mean of normalized counts
1e+00
1e+02
1e+04
1e+06
B
static (background)
upregulate (0.029)
downregulate (0.392)
Cumulative fraction of genes
Rank of genes based on regulatory Potential Score
(from high to low)
C
GO Biological Process
Binomial Region Hits
gland development
response to radiation
regulation of epithelial cell proliferation
regulation of cellular response to growth factor stimulus
response to corticosteroid
response to glucocorticoid
negative regulation of Notch signaling pathway
response to fibroblast growth factor
cellular response to fibroblast growth factor stimulus
fibroblast growth factor receptor signaling pathway
FDR = 5.5e-62
FDR = 9.4e-02
FDR = 2.7e-52
FDR = 8.21e-30
FDR = 2.4e-36
FDR = 8.76e-38
FDR = 5.2e-135
FDR = 1.7e-28
FDR = 8.8e-30
FDR = 2.9e-26
D
Cytosol
Membrane
Nuclear
Chromatin bound
FGF2 (5ng/ml)
Erdafitinib (250 nM)
FGFR1
Tubulin α/β
AIF
Lamin A/C
Histone H3
E
INPUT
FGFR1:IP
IgG:IP
FGF2 (5ng/ml)
Erdafitinib (250 nM)
Pol II S5P
FGFR1
F
FGFR1: ChIP
FGF2
FGF2 + erdafitinib
10 Kb

**Figure 6. Nuclear FGFR1 activity is enhanced by FGF2 but not affected by receptor tyrosine kinase blockade.** (A) MA plot of M (log ratio) versus A (log mean average) normalized counts, showing differentially expressed genes with *p* <1e-5 in response to FGF2 (5 ng/ml, 6 h). (B) Prediction of activating or repressing transcription function of FG2-stimulated FGFR1 by BETA platform. FGFR1 ChIP-Seq results from CAMA1 cells stimulated with FGF2 (5 ng/ml, 3 h) and RNA-Seq data from A were integrated. Genomic regions bound by FGFR1 are predicted to modulate expression of genes upregulated upon FGF2 stimulation, but not downregulated genes; *p* values indicate the significance of the associations compared to background non-regulated genes. (C) GREAT analysis the FGFR1 DNA binding sites identified by FGFR1 ChIP-Seq in CAMA1 cells stimulated with FGF2 (5 ng/ml, 3 h). Top ten enriched Gene Ontology (GO) Biological Processes and binomial FDR values are shown. (D) Subcellular fractionation on CAMA1 cells, showing FGFR1 in cytosolic, membrane, soluble nuclear and chromatin bound compartments, after treatment with FGF2 (5 ng/ml, 3h) ± erdafitinib (250 nM, 3h). Red box shows longer exposure. (E) Co-precipitation of FGFR1 and Pol II S5P from sonicated and nuclease-treated lysates of CAMA1 cells ± FGF2 (5 ng/ml, 3h) ± erdafitinib (250 nM, 3h). (F) Heatmaps of ChIP-Seq read densities around the FGFR1-bound regions in CAMA1 cells treated with FGF2 (5 ng/ml, 3h) ± erdafitinib (250 nM, 3h).

# 7. Supplementary Figures

**Supplementary Figure 1**

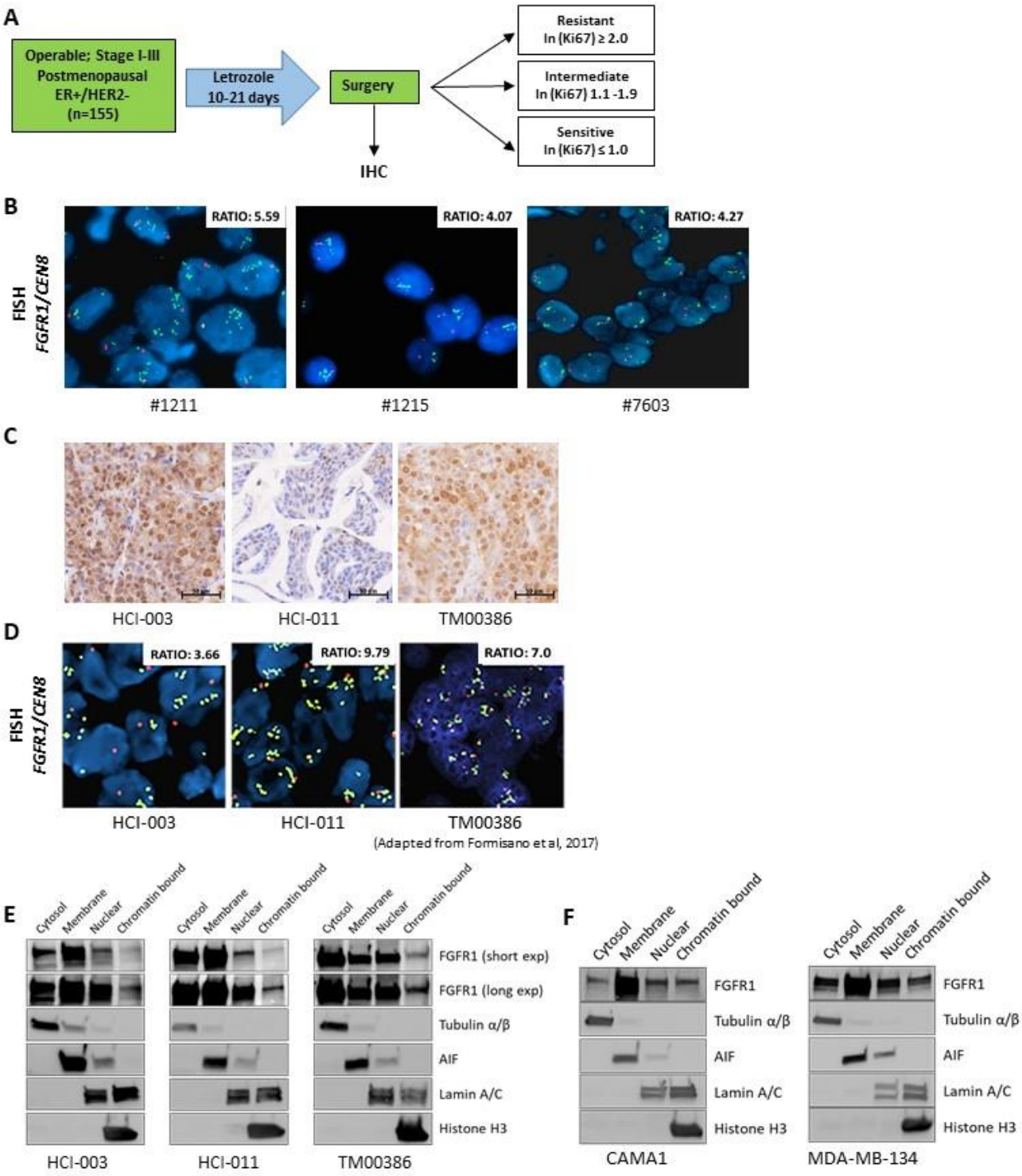

**Supplementary figure 1. FGFR1 is abundant in the nucleus of ER+/*FGR1*-amplified breast cancer cells.** (A) Schematic representation of the NCT00651976 trial (Refs. 12, 24). Patients with stage I-III, ER+/HER2– breast cancer received letrozole for 10–21 days immediately prior to surgery. Tumor response was categorized by calculating the natural log (ln) of the on-treatment Ki67 score, as determined by IHC. (B) Fluorescence *in situ* hybridization (FISH) on FFPE sections of ER+/*FGFR1*-amplified primary breast tumors and (D) HCI-003, HCI-011 and TM00386 PDXs. The *FGFR1:CEN8* ratio is indicated in the top right boxes. (C) Sections of FFPE of the HCI-003, HCI-011 and TM00386 ER+/*FGFR1*-amplified breast cancer PDXs were subjected to IHC with an FGFR1 antibody as described in the method. (E) Subcellular fractionation of HCI-003, HCI-011 and TM00386 PDXs and (F) ER+/*FGFR1*-amplified CAMA1 and MDA-MB-134 human breast cancer cells, showing distribution of FGFR1 across cytosolic, membrane, soluble nuclear and chromatin bound compartments. Other indicated proteins represent markers of different cellular compartments.

**Supplementary Figure 2**

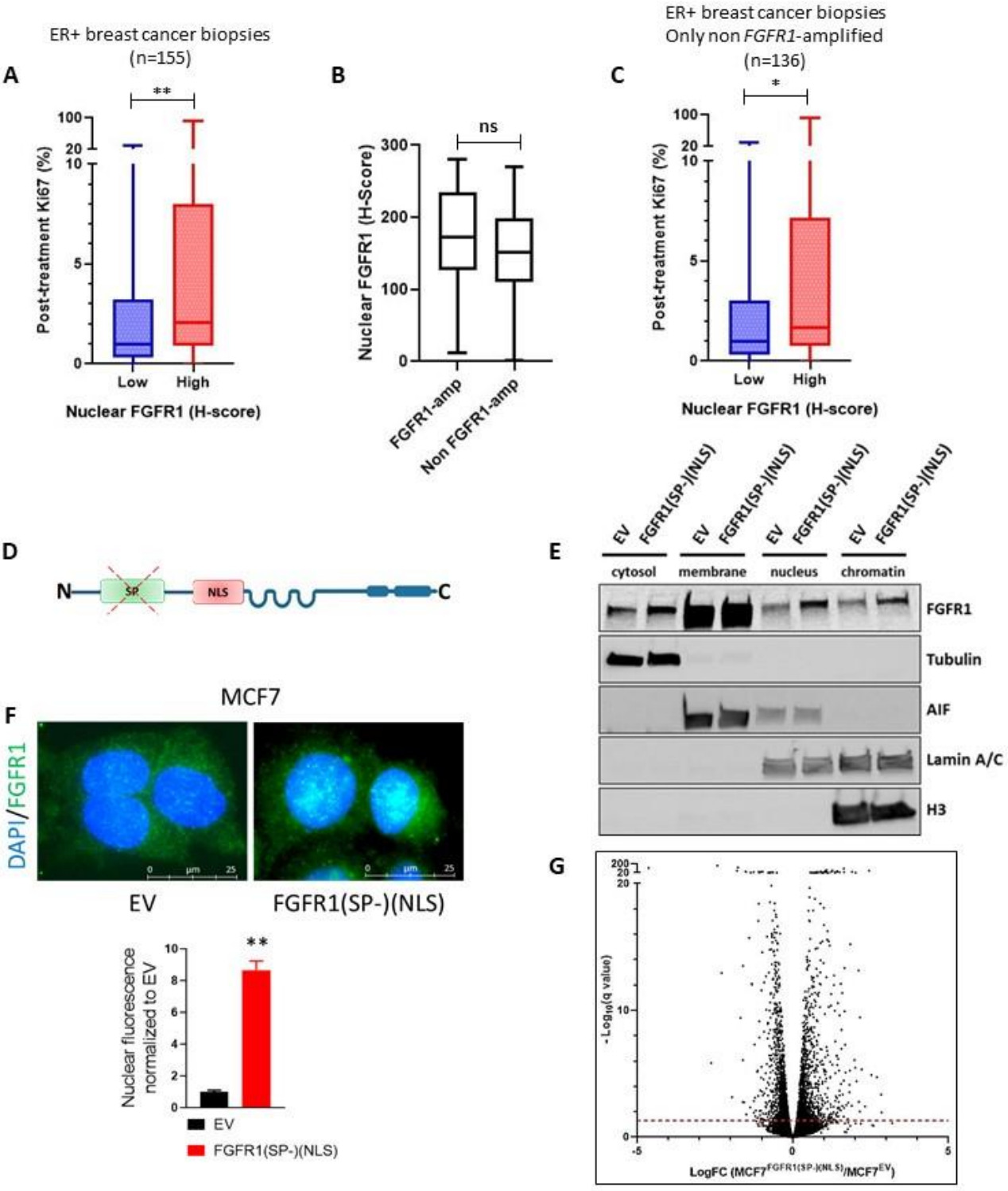

**Supplementary figure 2. Nuclear FGFR1 promotes antiestrogen resistance.** (A) Post-letrozole Ki67 values from the cohort of 155 ER+ primary breast cancer biopsies listed in Supplementary Table S1 as function of nuclear FGFR1 H-Score (high, n=78; low, n=77; ** $p$=0.0055, two-tailed Mann-Whitney test). (B) Nuclear FGFR1 H-Score in FGFR1-amplified (n=19) and non FGFR1-amplified (n=136) ER+ breast cancers from the cohort of 155 biopsies in A. (C) Post-letrozole Ki67 values from the non FGFR1-amplified biopsies (n=136) in A, as function of nuclear FGFR1 H-Score (high, n=68; low, n=68; ** $p$=0.027, two-tailed Mann-Whitney test). (D) Schematic representation of the FGFR1 peptide sequence for the FGFR1(SP-)(NLS) plasmid. (E) Subcellular fractionation of MCF-7$^{EV}$ and MCF-7$^{FGFR1(SP-)(NLS)}$ cells, showing distribution of FGFR1 across cytosolic, membrane, soluble nuclear and chromatin bound compartments. (F) Immunofluorescence (IF) with a primary rabbit FGFR1 antibody, followed by staining with a secondary goat anti-rabbit antibody (Alexa Fluor 488) and DAPI was performed in MCF7$^{EV}$ and MCF7$^{FGFR1(SP-)(NLS)}$ cells. Nuclear localization of FGFR1 was detected by confocal microscopy. Bar graph representing the mean nuclear FGFR1 fluorescent signals ± SD of 3 areas. Nuclear FGFR1 fluorescence was quantified using the software ImageJ (* Two-tailed t-test, $p$=0.0013). (G) Volcano plot analysis of differentially expressed genes in MCF7$^{FGFR1(SP-)(NLS)}$ vs MCF7$^{EV}$ cells (n=3 replicates). The red dashed line indicates FDR=0.05.

**Supplementary Figure 3**

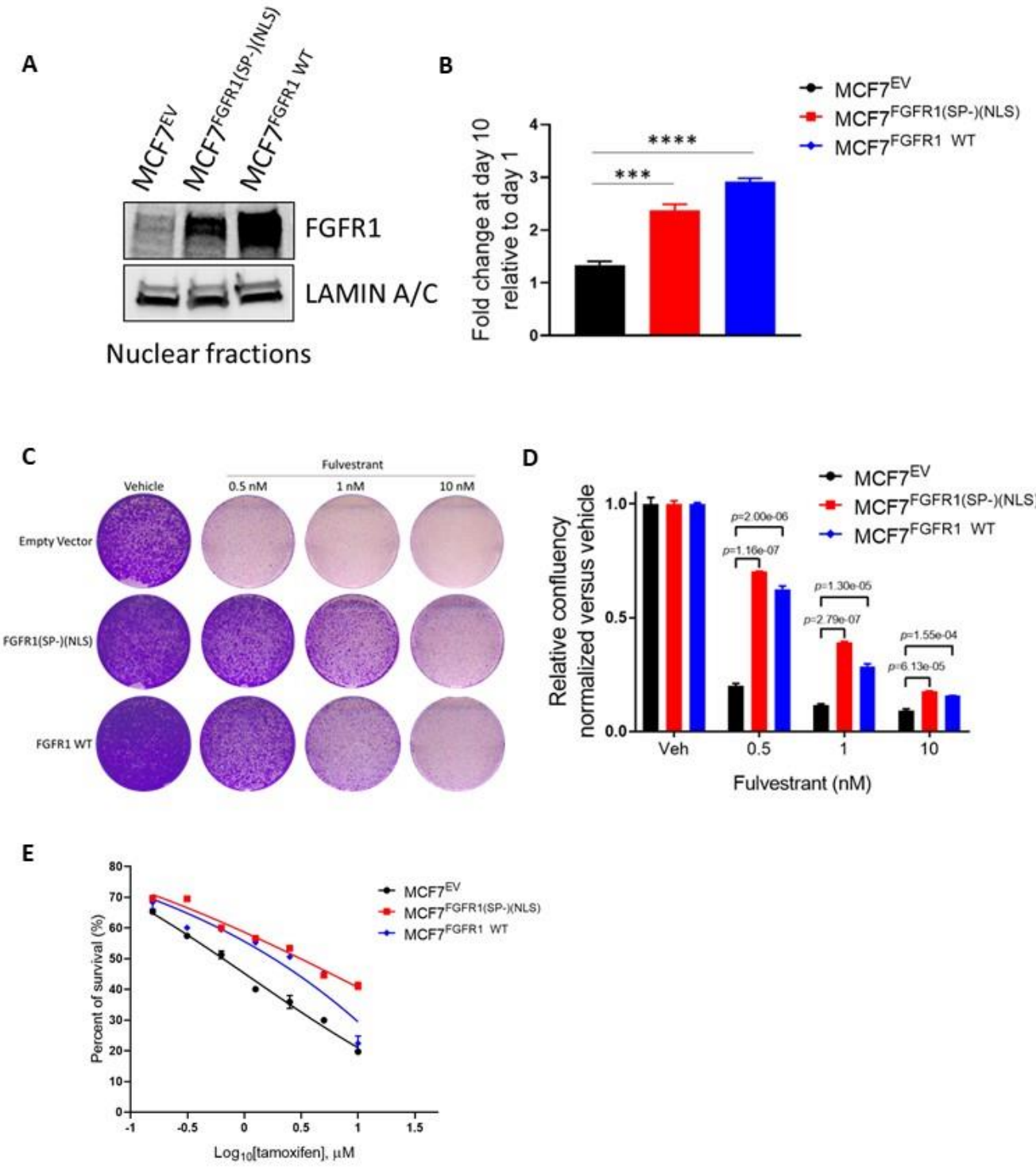

**Supplementary figure 3. Overexpression of FGFR1(SP-)(NLS) and wild-type FGFR1 confers antiestrogen resistance.** (A) Western blot showing the levels of FGFR1 in nuclear fractions of $MCF7^{EV}$, $MCF7^{FGFR1(SP-)(NLS)}$ and $MCF7^{FGFR1\ WT}$ cells (B) Cells were seeded in 6-well plates in estrogen-deprived media. Media was replenished every 72 hours. Monolayers were stained with crystal violet on days 1 and 10. Quantification of the integrated intensity values as fold change normalized to day 1 (Two-tailed t-test, *** $p$=0.0005, **** $p$<0.0001). (C) Cells were seeded in 6-well plates in full media and treated with vehicle (DMSO) or fulvestrant. After seven days, monolayers were stained with crystal violet. (D) Quantification of the integrated intensity values as fold change normalized to vehicle-treated controls (Multiple Student's t-test). (E) Dose-response curves of $MCF7^{EV}$, $MCF7^{FGFR1(SP-)(NLS)}$ and $MCF7^{FGFR1\ WT}$ cells treated with tamoxifen. Cells were seeded in 24-well plates. After 6 days of treatment, monolayers were stained with crystal violet and cell number measured as described in Methods. Each data point represents the percentage of cell viability relative to vehicle-treated controls. Mean viability ± SD from three independent replicates are shown.

**Supplementary Figure 4**

A

| | Motif | % of Target Sequences with motif | % of Background Sequences with motif | p-value |
|---|---|---|---|---|
|  | SP1 | 44,3 | 26.2 | 1e-147 |
|  | ELK1 | 25.8 | 12.7 | 1e-121 |
|  | NFY (CCAAT) | 13.35 | 6.54 | 1e-59 |
|  | NRF | 11.83 | 6.2 | 1e-42 |
|  | BORIS | 8.99 | 2.25 | 1e-116 |
|  | SREBF2 | 4.68 | 1.26 | 1e-55 |
|  | GFY | 2.63 | 0.99 | 1e-19 |
|  | TBP | 2.83 | 0.59 | 1e-44 |

**Supplementary figure 4. Nuclear FGFR1 associates with GC-rich DNA sequences.** (A) List of the top enriched motifs identified at FGFR1-bound genomic loci, as described in methods. Percent (%) of target sequences with motif, percent (%) of background sequences with motif and *p*-values are shown.

**Supplementary Figure 5**

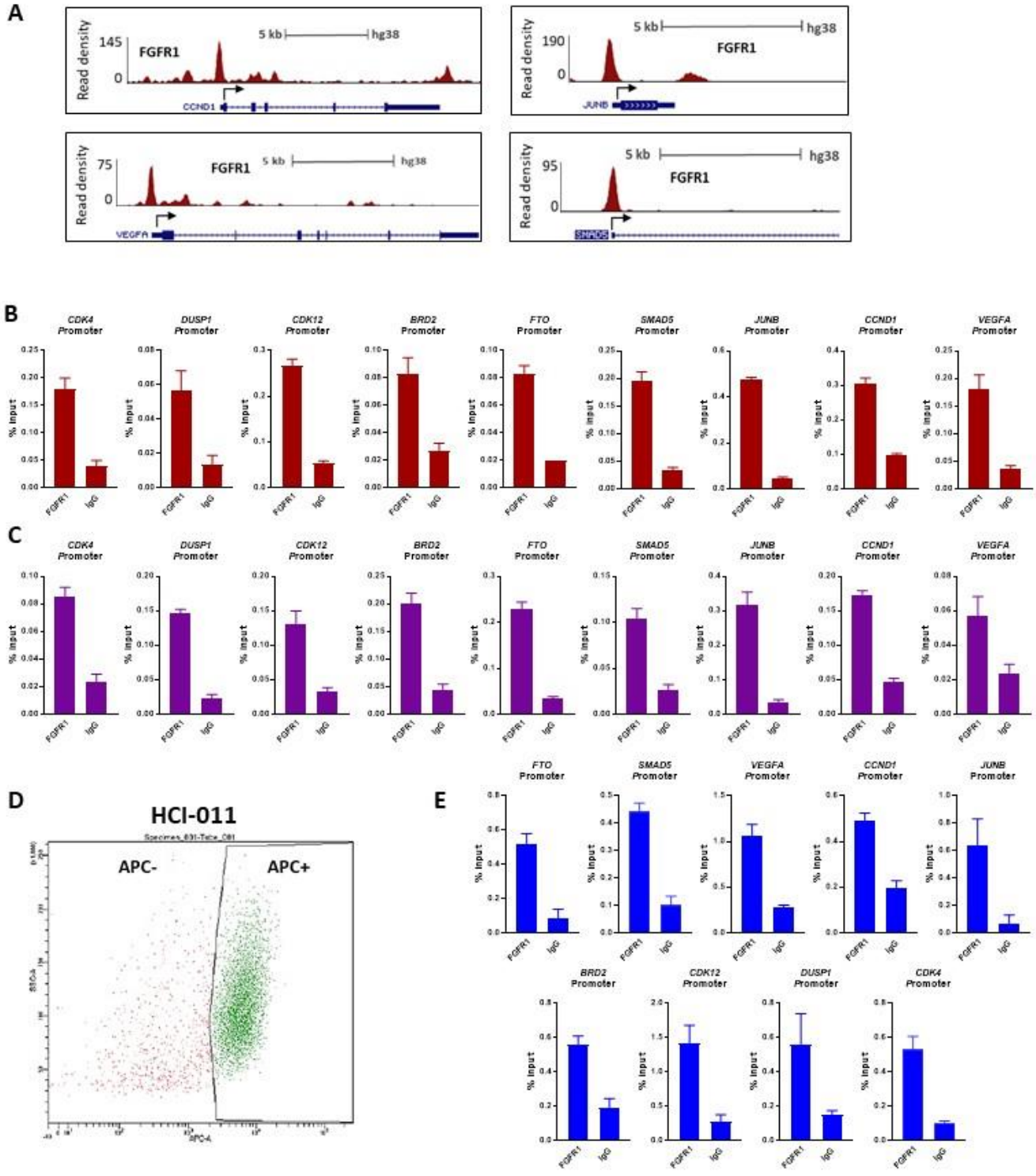

**Supplementary figure 5. Nuclear FGFR1 occupies chromatin at transcription start sites.** (A) Distribution of FGFR1 binding peaks at the *CCND1, JUNB, VEGFA* and *SMAD5* promoters (UCSC genome browser). (B) ChIP-qPCR validating the binding of FGFR1 at the *CDK4, DUSP1, CDK12, BRD2, FTO, SMAD5, JUNB, CCND1,* and *VEGFA* promoters in CAMA1, (C) MDA-MB-134 and (E) HCI-011 PDX-derived cells. Enrichment values expressed as percent (%) of input. (D) Fluorescence-activated cell sorting (FACS) analysis conducted on HCI-011 PDX-derived cells. After mechanical and enzymatic digestion, PDX-derived cell suspensions were fixed with 4% PFA and stained with APC-CD298 antibody, in order to isolate human epithelial cells.

**Supplementary Figure 6**

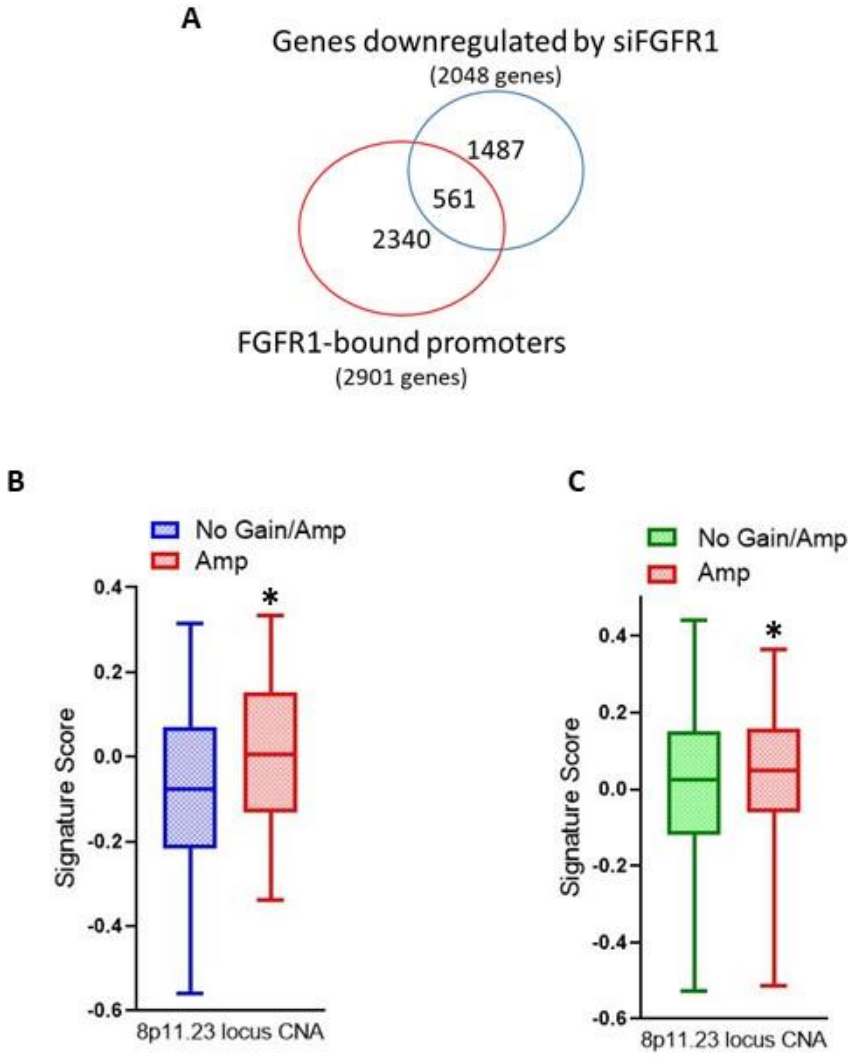

**Supplementary figure 6. FGFR1-associated polygenic risk score correlates with *FGFR1* gene copy number.** (A) Venn diagram of genes whose promoter is bound by FGFR1, as identified by ChIP-Seq and genes down-regulated by FGFR1 siRNA in CAMA1 cells. (B) Plot of the values for FGFR1-associated risk score, calculated by GSVA based on the 561 overlapping genes in A, in 212 ER+/HER2- breast cancers in TCGA with known 8p11.23 copy number. Samples were stratified based on 8p11.23 copy number alteration (* Two-tailed t-test $p$=0.039). (C) Plot of the values for the FGFR1-associated risk score in 1294 ER+/HER2- breast cancers in METABRIC. Samples were stratified based on 8p11.23 copy number alteration (* Two-tailed t-test $p$=0.038).

**Supplementary Figure 7**

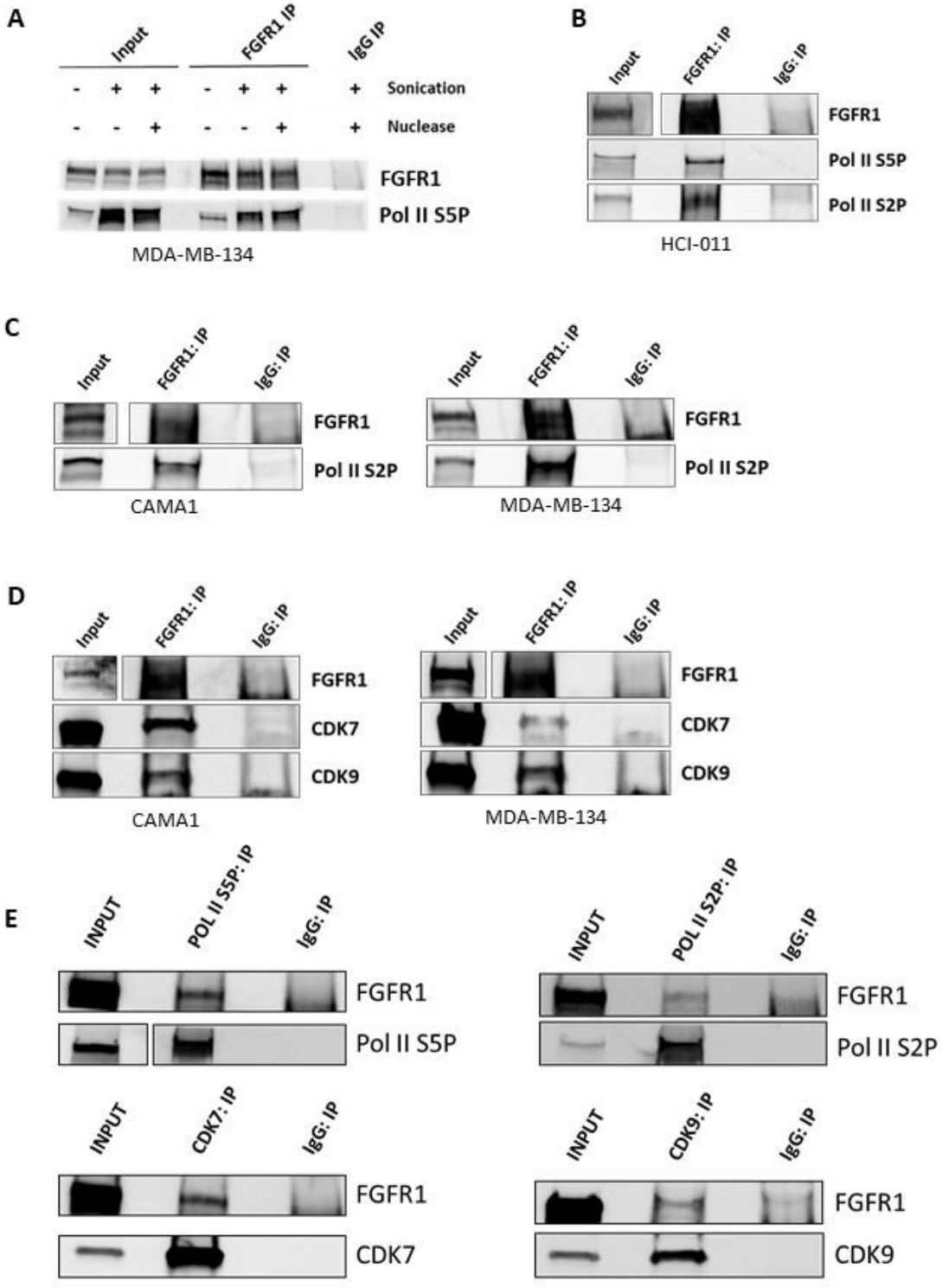

**Supplementary figure 7. FGFR1 associates with RNA Polymerase II.** (A) Co-precipitation of FGFR1 and Pol II S5P, with or without sonication and nuclease treatment in MDA-MB134 cells. (B) Co-precipitation of FGFR1, Pol II S5P and Pol II S2P in sonicated and nuclease treated HCI-011 PDX lysates. (C) Co-precipitation of FGFR1 and Pol II S2P in sonicated and nuclease treated CAMA1 (left panel) and MDA-MB-134 (right panel) cell lysates. (D) Co-precipitation of FGFR1, CDK7 and CDK9, in sonicated and nuclease treated CAMA1 (left panel) and MDA-MB134 (right panel) cell lysates. (E) Immunoprecipitation assays with Pol II S5P, Pol II S2P, CDK7 and CDK9 antibodies, followed by western blot analysis for FGFR1 in CAMA1 cells.

**Supplementary Figure 8**

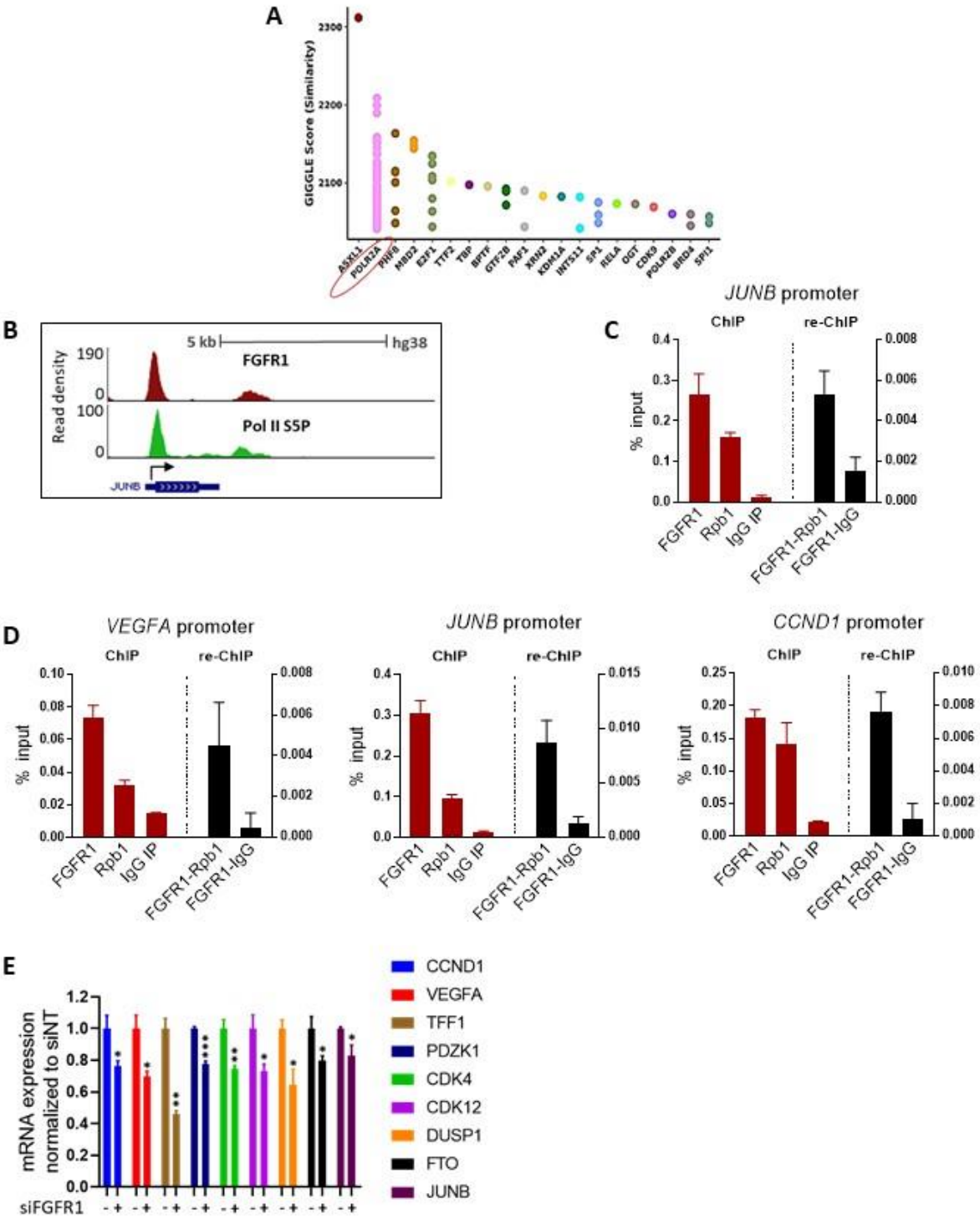

**Supplementary figure 8. FGFR1 – Pol II association occurs at transcription start sites.** (A) Similarity (GIGGLE) scores between FGFR1 peaks identified in CAMA1 cells and GEO-archived datasets of ChIP-Seq for transcription factors. Data was obtained using "Cistrome Toolkit" (http://dbtoolkit.cistrome.org/). Each point represents one ChIP-Seq dataset. (B) Distribution of FGFR1 and Pol II S5P binding peaks at the *JUNB* promoter (UCSC genome browser). (C) ChIP-reChIP assay performed by sequential ChIP-qPCR with an FGFR1 antibody followed by a Pol II S5P antibody or normal rabbit IgG at the *JUNB* promoter in CAMA1 cells and (D) *JUNB, CCND1,* and *VEGFA* promoters in MDA-MB-134 cells. (E) CAMA1 cells were transfected with non-targeting siRNA (siNT) or siFGFR1 in 60 mm dishes. Seventy-two h post-transfection, cells were collected for RNA extraction. The expression of selected mRNAs was evaluated by RT-qPCR. Each bar represents the mean ± SD $2^{-\Delta\Delta CT}$ values of selected mRNAs normalized to CAMA1 siNT in 3 replicates (Two-tailed t-test, * $p$<0.05, ** $p$<0.005, *** $p$<0.0005).

**Supplementary Figure 9**

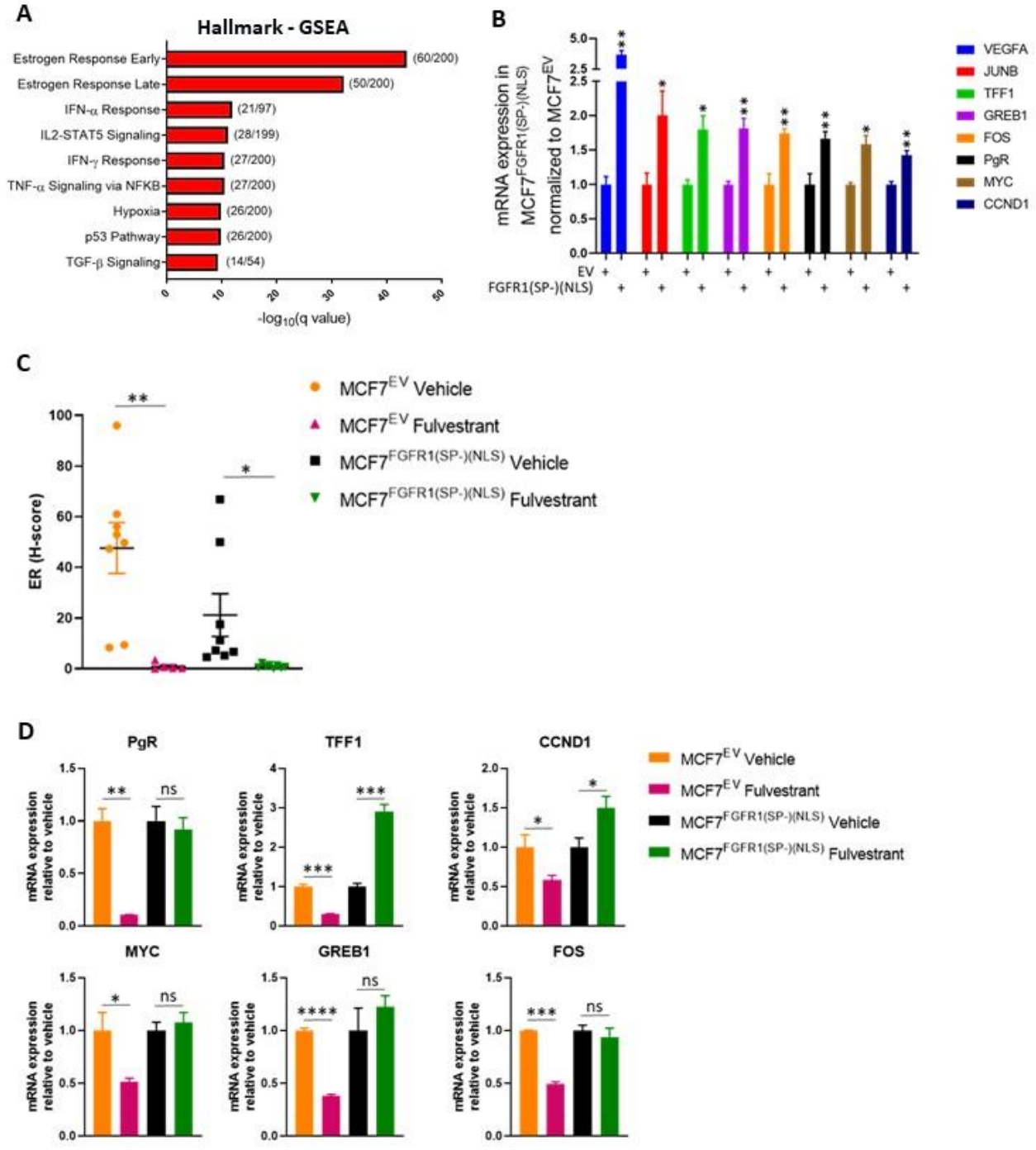

**Supplementary figure 9. Nuclear FGFR1 promotes the expression of canonical ERα target genes.** (A) Hallmark GSEA of 1009 genes upregulated in MCF7$^{FGFR1(SP-)(NLS)}$ vs MCF7$^{EV}$ and bound by FGFR1 as shown in figure 3I. Top 8 enriched gene sets are shown. Gene sets are ranked based on $-\log_{10}$(q value). Ratio between number of upregulated genes included in the respective gene set and total number of genes for each set is included in parentheses. (B) RT-qPCR to evaluate the expression of VEGFA, JUNB, TFF1, GREB1, FOS, PgR, MYC and CCND1 mRNAs in MCF7$^{FGFR1(SP-)(NLS)}$ cells vs. MCF7$^{EV}$ cells. Each bar represents the mean ± SD $2^{-\Delta\Delta CT}$ values of selected mRNAs normalized to MCF7$^{EV}$ in 3 replicates (Two-tailed t-test, * $p$<0.05, ** $p$<0.005). (C) MCF7$^{FGFR1(SP-)(NLS)}$ and MCF7$^{EV}$ xenografts were harvested after 4 weeks of treatment with vehicle or fulvestrant. FFPE tumor sections were prepared and subjected to ERα IHC. The percent of ERα+ tumor cells and staining intensity were assessed to generate an H-Score (Two-tailed t-test, * $p$<0.05, ** $p$<0.005). (D) RT-qPCR was used to evaluate the expression of PgR, TFF1, CCND1, MYC, GREB1 and FOS mRNAs in MCF7$^{EV}$ and MCF7$^{FGFR1(SP-)(NLS)}$ xenografts harvested and snap-frozen after 4 weeks of treatment with vehicle or fulvestrant. Each bar represents the mean ± SD $2^{-\Delta\Delta CT}$ values of selected mRNAs normalized to vehicle in 3 replicates (Two-tailed t-test, * $p$<0.05, ** $p$<0.005, *** $p$<0.0005, **** $p$<0.0001).

**Supplementary Figure 10**

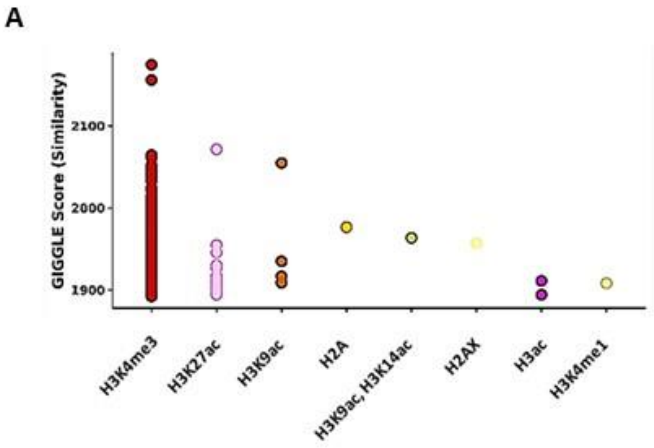


**Supplementary figure 10. Nuclear FGFR1 overlaps with active transcription marks.** (A) Similarity (GIGGLE) scores between FGFR1 peaks identified in CAMA1 cells in Figure 2A and GEO-archived datasets of ChIP-Seq for histone marks. Data obtained using “Cistrome Toolkit” (http://dbtoolkit.cistrome.org/). Each point represents one ChIP-Seq dataset.

**Supplementary Figure 11**

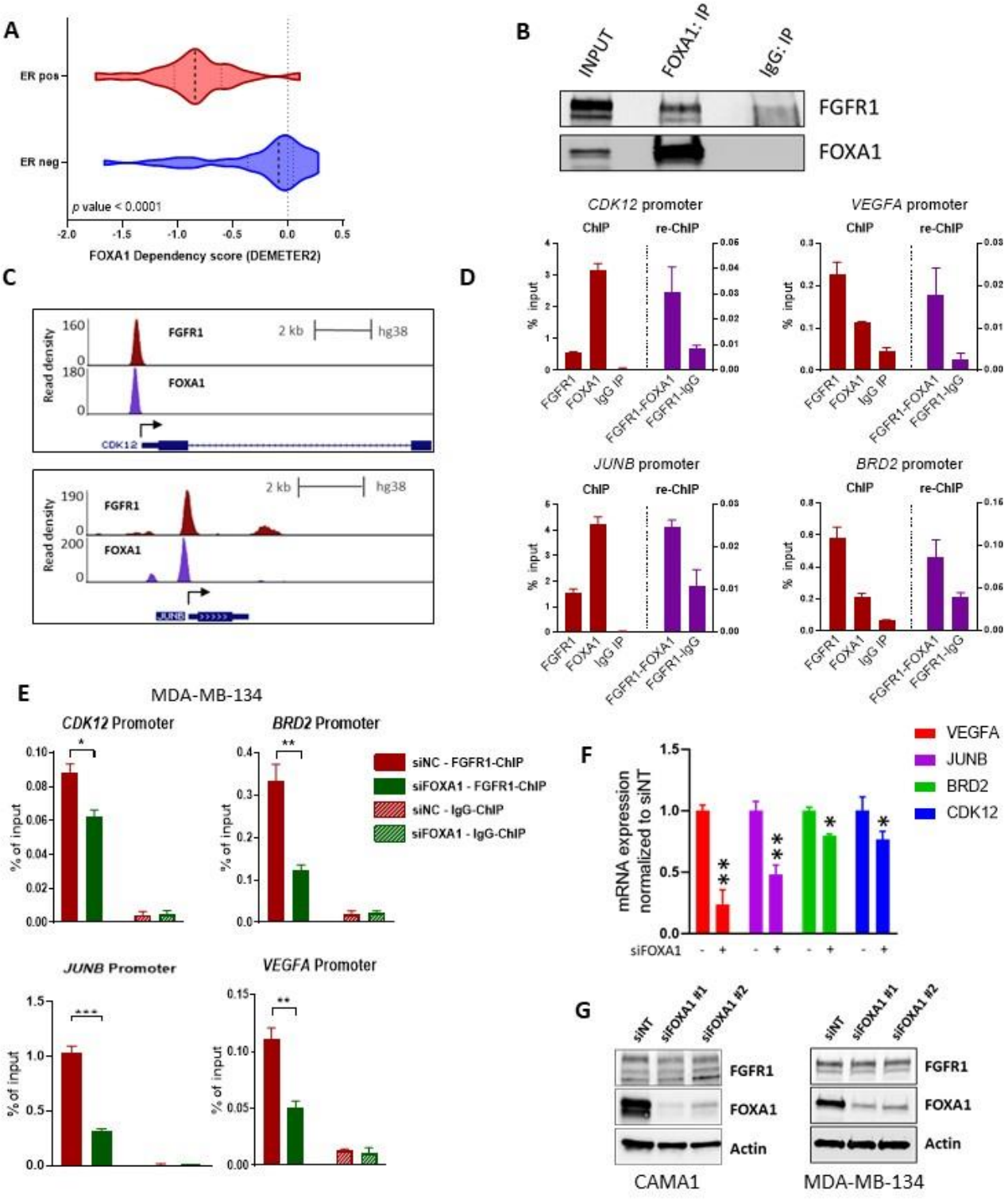

**Supplementary figure 11. FOXA1 mediates FGFR1 recruitment to chromatin.** (A) FOXA1 dependency score calculated in ER- (n=40) and ER+ (n=21) breast cancer cell lines based on the DEMETER2 scoring system (https://depmap.org/portal/) (Two-tailed t-test). (B) Immunoprecipitation assay with a FOXA1 antibody, followed by western blot analysis for FGFR1 in CAMA1 cells. (C) Distribution of FGFR1 and FOXA1 binding peaks at the *JUNB* and *CDK12* promoters in CAMA1 cells (UCSC genome browser). (D) ChIP-reChIP assay performed by sequential ChIP-qPCR with an FGFR1 antibody followed by a FOXA1 antibody or normal rabbit IgG at the *CDK12, BRD2*, *JUNB* and *VEGFA* promoters in MDA-MB-134 cells. Enrichment values expressed as percent (%) of input. (E) ChIP-qPCR confirmation of reduced FGFR1 binding at the *CDK12, BRD2, VEGFA* and *JUNB* promoters in MDA-MB-134 cells ± FOXA1 siRNA (Two-tailed t-test, * $p<0.05$, ** $p<0.005$, *** $p<0.0005$). Cells were collected 72 h post-transfection. (F) CAMA1 cells were transfected with non-targeting siRNA (siNT) or siFOXA1 in 60 mm dishes. Seventy-two h post-transfection, cells were collected for RNA extraction. The expression of selected mRNAs was evaluated by RT-qPCR. Each bar represents the mean ± SD $2^{-\Delta\Delta CT}$ values of selected mRNAs normalized to CAMA1 siNT in 3 replicates (Two-tailed t-test, * $p<0.05$, ** $p<0.005$). (G) Western blot showing FGFR1, FOXA1 and Actin levels in CAMA1 (left panel) and MDA-MB-134 (right panel) cells transfected with non-targeting control siRNA and siFOXA1. Cells were collected 72 h post-transfection.

**Supplementary Figure 12**

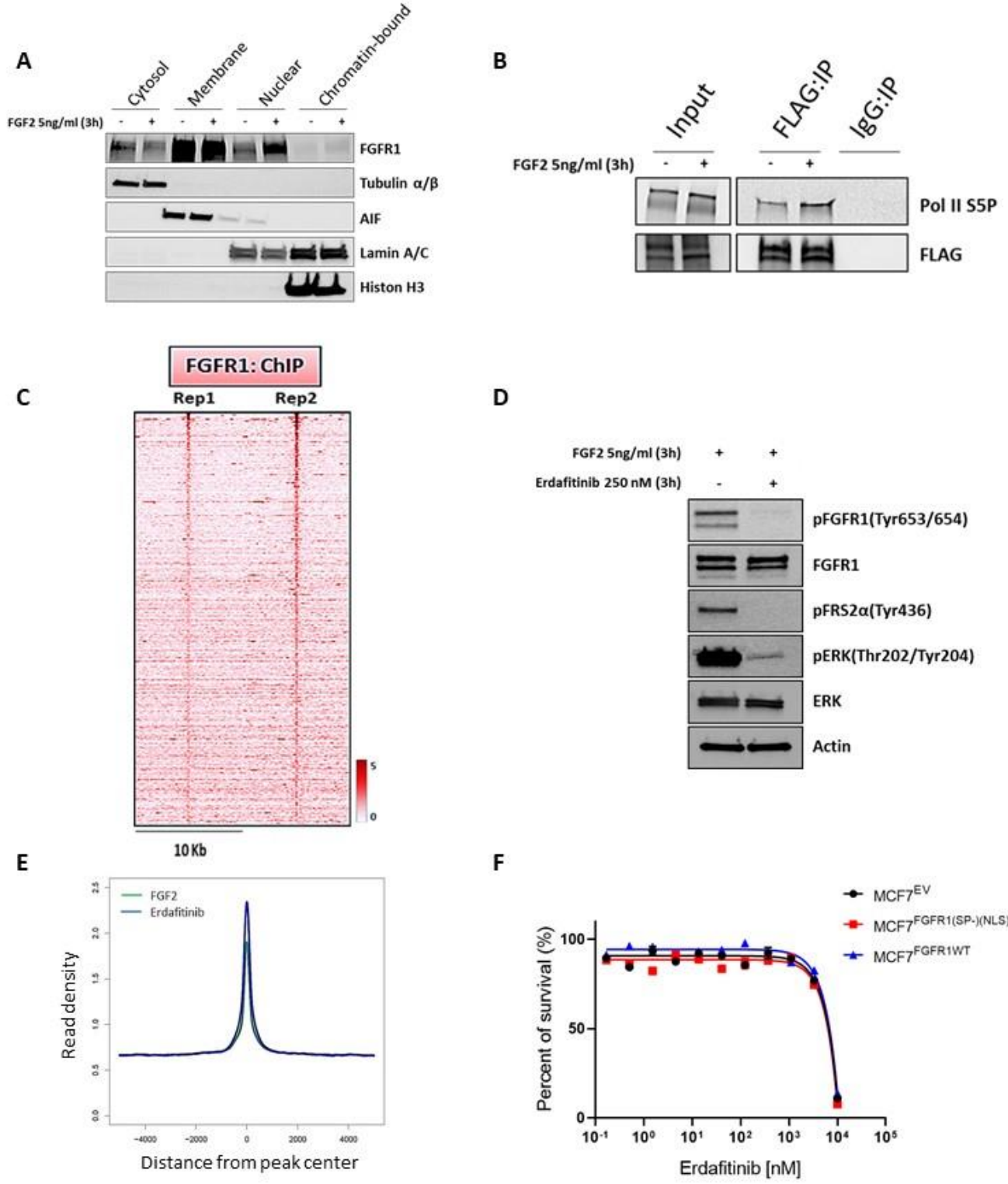

**Supplementary figure 12. Nuclear FGFR1 activity is not affected by receptor tyrosine kinase blockade.** (A) Subcellular fractionation of CAMA1 cells, showing FGFR1 in cytosolic, membrane, soluble nuclear and chromatin bound compartments, after stimulation with FGF2 (5 ng/ml, 3 h). (B) Co-precipitation of FLAG-FGFR1 and Pol II S5P, after treatment with FGF2 (5 ng/ml, 3 h), from sonicated- and nuclease-treated lysates of CAMA1$^{3XFLAG\text{-}FGFR1}$ cells. (C) Heatmap showing ChIP-Seq read densities around the FGFR1-bound regions in CAMA1 cells after stimulation with FGF2 (5 ng/ml, 3 h), in two replicates. The x-axis represents read densities within 10-kb of the peak summit; the y-axis represents each predicted binding site. (D) Immunoblot analysis of CAMA1 cells lysates after treatment with FGF2 (5 ng/ml, 3h) ± erdafitinib (250 nM, 3h). (E) Plot representing the density of the FGFR1 distribution around the peak center, identified by ChIP-Seq shown in Figure 6F. (F) Dose-response curves of MCF7$^{EV}$, MCF7$^{FGFR1(SP-)(NLS)}$ and MCF7$^{FGFR1\ WT}$ cells treated with erdafitinib. Cells were seeded in 12-well plates in triplicate. After 6 days of treatment, monolayers were stained with crystal violet and cell number measured as described in Methods. Each data point represents the percentage of cell viability relative to vehicle-treated controls. Mean viability ± SD from three independent replicates are shown.

# 8. References


1. Turner N, Grose R. Fibroblast growth factor signalling: from development to cancer. *Nat Rev Cancer* 2010;**10**(2):116-29 doi 10.1038/nrc2780.
2. Schlessinger J, Plotnikov AN, Ibrahimi OA, Eliseenkova AV, Yeh BK, Yayon A*, et al.* Crystal structure of a ternary FGF-FGFR-heparin complex reveals a dual role for heparin in FGFR binding and dimerization. *Mol Cell* 2000;**6**(3):743-50 doi 10.1016/s1097-2765(00)00073-3.
3. Eswarakumar VP, Lax I, Schlessinger J. Cellular signaling by fibroblast growth factor receptors. *Cytokine Growth Factor Rev* 2005;**16**(2):139-49 doi 10.1016/j.cytogfr.2005.01.001.
4. Peters KG, Marie J, Wilson E, Ives HE, Escobedo J, Del Rosario M*, et al.* Point mutation of an FGF receptor abolishes phosphatidylinositol turnover and Ca2+ flux but not mitogenesis. *Nature* 1992;**358**(6388):678-81 doi 10.1038/358678a0.
5. Klint P, Claesson-Welsh L. Signal transduction by fibroblast growth factor receptors. *Front Biosci* 1999;**4**:D165-77 doi 10.2741/klint.
6. Hart KC, Robertson SC, Kanemitsu MY, Meyer AN, Tynan JA, Donoghue DJ. Transformation and Stat activation by derivatives of FGFR1, FGFR3, and FGFR4. *Oncogene* 2000;**19**(29):3309-20 doi 10.1038/sj.onc.1203650.
7. Reis-Filho JS, Simpson PT, Turner NC, Lambros MB, Jones C, Mackay A*, et al.* FGFR1 emerges as a potential therapeutic target for lobular breast carcinomas. *Clin Cancer Res* 2006;**12**(22):6652-62 doi 10.1158/1078-0432.CCR-06-1164.
8. Yang W, Yao YW, Zeng JL, Liang WJ, Wang L, Bai CQ*, et al.* Prognostic value of FGFR1 gene copy number in patients with non-small cell lung cancer: a meta-analysis. *J Thorac Dis* 2014;**6**(6):803-9 doi 10.3978/j.issn.2072-1439.2014.05.02.
9. Gorringe KL, Jacobs S, Thompson ER, Sridhar A, Qiu W, Choong DY*, et al.* High-resolution single nucleotide polymorphism array analysis of epithelial ovarian cancer reveals numerous microdeletions and amplifications. *Clin Cancer Res* 2007;**13**(16):4731-9 doi 10.1158/1078-0432.CCR-07-0502.
10. Simon R, Richter J, Wagner U, Fijan A, Bruderer J, Schmid U*, et al.* High-throughput tissue microarray analysis of 3p25 (RAF1) and 8p12 (FGFR1) copy number alterations in urinary bladder cancer. *Cancer Res* 2001;**61**(11):4514-9.
11. Cancer Genome Atlas N. Comprehensive molecular portraits of human breast tumours. *Nature* 2012;**490**(7418):61-70 doi 10.1038/nature11412.
12. Giltnane JM, Hutchinson KE, Stricker TP, Formisano L, Young CD, Estrada MV*, et al.* Genomic profiling of ER(+) breast cancers after short-term estrogen suppression reveals alterations associated with endocrine resistance. *Sci Transl Med* 2017;**9**(402) doi 10.1126/scitranslmed.aai7993.
13. Babina IS, Turner NC. Advances and challenges in targeting FGFR signalling in cancer. *Nat Rev Cancer* 2017;**17**(5):318-32 doi 10.1038/nrc.2017.8.
14. Coleman SJ, Chioni AM, Ghallab M, Anderson RK, Lemoine NR, Kocher HM*, et al.* Nuclear translocation of FGFR1 and FGF2 in pancreatic stellate cells facilitates pancreatic cancer cell invasion. *EMBO Mol Med* 2014;**6**(4):467-81 doi 10.1002/emmm.201302698.

15. Chioni AM, Grose R. FGFR1 cleavage and nuclear translocation regulates breast cancer cell behavior. *J Cell Biol* 2012;**197**(6):801-17 doi 10.1083/jcb.201108077.

16. Terranova C, Narla ST, Lee YW, Bard J, Parikh A, Stachowiak EK*, et al.* Global Developmental Gene Programing Involves a Nuclear Form of Fibroblast Growth Factor Receptor-1 (FGFR1). *PLoS One* 2015;**10**(4):e0123380 doi 10.1371/journal.pone.0123380.

17. Fang X, Stachowiak EK, Dunham-Ems SM, Klejbor I, Stachowiak MK. Control of CREB-binding protein signaling by nuclear fibroblast growth factor receptor-1: a novel mechanism of gene regulation. *J Biol Chem* 2005;**280**(31):28451-62 doi 10.1074/jbc.M504400200.

18. Carpenter G, Liao HJ. Receptor tyrosine kinases in the nucleus. *Cold Spring Harb Perspect Biol* 2013;**5**(10):a008979 doi 10.1101/cshperspect.a008979.

19. Hancock ML, Meyer RC, Mistry M, Khetani RS, Wagschal A, Shin T*, et al.* Insulin Receptor Associates with Promoters Genome-wide and Regulates Gene Expression. *Cell* 2019;**177**(3):722-36 e22 doi 10.1016/j.cell.2019.02.030.

20. Redmond AM, Omarjee S, Chernukhin I, Le Romancer M, Carroll JS. Analysis of HER2 genomic binding in breast cancer cells identifies a global role in direct gene regulation. *PLoS One* 2019;**14**(11):e0225180 doi 10.1371/journal.pone.0225180.

21. Lin SY, Makino K, Xia W, Matin A, Wen Y, Kwong KY*, et al.* Nuclear localization of EGF receptor and its potential new role as a transcription factor. *Nat Cell Biol* 2001;**3**(9):802-8 doi 10.1038/ncb0901-802.

22. Drago JZ, Formisano L, Juric D, Niemierko A, Servetto A, Wander SA*, et al.* FGFR1 Amplification Mediates Endocrine Resistance but Retains TORC Sensitivity in Metastatic Hormone Receptor-Positive (HR(+)) Breast Cancer. *Clin Cancer Res* 2019;**25**(21):6443-51 doi 10.1158/1078-0432.CCR-19-0138.

23. Turner N, Pearson A, Sharpe R, Lambros M, Geyer F, Lopez-Garcia MA*, et al.* FGFR1 amplification drives endocrine therapy resistance and is a therapeutic target in breast cancer. *Cancer Res* 2010;**70**(5):2085-94 doi 10.1158/0008-5472.CAN-09-3746.

24. Formisano L, Stauffer KM, Young CD, Bhola NE, Guerrero-Zotano AL, Jansen VM*, et al.* Association of FGFR1 with ERalpha Maintains Ligand-Independent ER Transcription and Mediates Resistance to Estrogen Deprivation in ER(+) Breast Cancer. *Clin Cancer Res* 2017;**23**(20):6138-50 doi 10.1158/1078-0432.CCR-17-1232.

25. Bankhead P, Loughrey MB, Fernandez JA, Dombrowski Y, McArt DG, Dunne PD*, et al.* QuPath: Open source software for digital pathology image analysis. *Sci Rep* 2017;**7**(1):16878 doi 10.1038/s41598-017-17204-5.

26. Camp RL, Chung GG, Rimm DL. Automated subcellular localization and quantification of protein expression in tissue microarrays. *Nat Med* 2002;**8**(11):1323-7 doi 10.1038/nm791.

27. Langmead B, Salzberg SL. Fast gapped-read alignment with Bowtie 2. *Nat Methods* 2012;**9**(4):357-9 doi 10.1038/nmeth.1923.

28. Li H, Handsaker B, Wysoker A, Fennell T, Ruan J, Homer N*, et al.* The Sequence Alignment/Map format and SAMtools. *Bioinformatics* 2009;**25**(16):2078-9 doi 10.1093/bioinformatics/btp352.

29. Zhang Y, Liu T, Meyer CA, Eeckhoute J, Johnson DS, Bernstein BE*, et al.* Model-based analysis of ChIP-Seq (MACS). *Genome Biol* 2008;**9**(9):R137 doi 10.1186/gb-2008-9-9-r137.

30. Heinz S, Benner C, Spann N, Bertolino E, Lin YC, Laslo P*, et al.* Simple combinations of lineage-determining transcription factors prime cis-regulatory elements required for macrophage and B cell identities. *Mol Cell* 2010;**38**(4):576-89 doi 10.1016/j.molcel.2010.05.004.

31. Shen L, Shao N, Liu X, Nestler E. ngs.plot: Quick mining and visualization of next-generation sequencing data by integrating genomic databases. *BMC Genomics* 2014;**15**:284 doi 10.1186/1471-2164-15-284.

32. Wolff AC, Hammond MEH, Allison KH, Harvey BE, Mangu PB, Bartlett JMS*, et al.* Human Epidermal Growth Factor Receptor 2 Testing in Breast Cancer: American Society of Clinical Oncology/College of American Pathologists Clinical Practice Guideline Focused Update. *Arch Pathol Lab Med* 2018;**142**(11):1364-82 doi 10.5858/arpa.2018-0902-SA.

33. Peng H, Moffett J, Myers J, Fang X, Stachowiak EK, Maher P*, et al.* Novel nuclear signaling pathway mediates activation of fibroblast growth factor-2 gene by type 1 and type 2 angiotensin II receptors. *Mol Biol Cell* 2001;**12**(2):449-62 doi 10.1091/mbc.12.2.449.

34. Sandelin A, Carninci P, Lenhard B, Ponjavic J, Hayashizaki Y, Hume DA. Mammalian RNA polymerase II core promoters: insights from genome-wide studies. *Nat Rev Genet* 2007;**8**(6):424-36 doi 10.1038/nrg2026.

35. Fenouil R, Cauchy P, Koch F, Descostes N, Cabeza JZ, Innocenti C*, et al.* CpG islands and GC content dictate nucleosome depletion in a transcription-independent manner at mammalian promoters. *Genome Res* 2012;**22**(12):2399-408 doi 10.1101/gr.138776.112.

36. Deaton AM, Bird A. CpG islands and the regulation of transcription. *Genes Dev* 2011;**25**(10):1010-22 doi 10.1101/gad.2037511.

37. Landolin JM, Johnson DS, Trinklein ND, Aldred SF, Medina C, Shulha H*, et al.* Sequence features that drive human promoter function and tissue specificity. *Genome Res* 2010;**20**(7):890-8 doi 10.1101/gr.100370.109.

38. Hahn S. Structure and mechanism of the RNA polymerase II transcription machinery. *Nat Struct Mol Biol* 2004;**11**(5):394-403 doi 10.1038/nsmb763.

39. Buratowski S. Progression through the RNA polymerase II CTD cycle. *Mol Cell* 2009;**36**(4):541-6 doi 10.1016/j.molcel.2009.10.019.

40. Komarnitsky P, Cho EJ, Buratowski S. Different phosphorylated forms of RNA polymerase II and associated mRNA processing factors during transcription. *Genes Dev* 2000;**14**(19):2452-60 doi 10.1101/gad.824700.

41. Jonkers I, Lis JT. Getting up to speed with transcription elongation by RNA polymerase II. *Nat Rev Mol Cell Biol* 2015;**16**(3):167-77 doi 10.1038/nrm3953.

42. Zheng R, Wan C, Mei S, Qin Q, Wu Q, Sun H*, et al.* Cistrome Data Browser: expanded datasets and new tools for gene regulatory analysis. *Nucleic Acids Res* 2019;**47**(D1):D729-D35 doi 10.1093/nar/gky1094.

43. Wang S, Sun H, Ma J, Zang C, Wang C, Wang J*, et al.* Target analysis by integration of transcriptome and ChIP-seq data with BETA. *Nat Protoc* 2013;**8**(12):2502-15 doi 10.1038/nprot.2013.150.

44. Heintzman ND, Stuart RK, Hon G, Fu Y, Ching CW, Hawkins RD*, et al.* Distinct and predictive chromatin signatures of transcriptional promoters and enhancers in the human genome. *Nat Genet* 2007;**39**(3):311-8 doi 10.1038/ng1966.

45. Roadmap Epigenomics C, Kundaje A, Meuleman W, Ernst J, Bilenky M, Yen A*, et al.* Integrative analysis of 111 reference human epigenomes. *Nature* 2015;**518**(7539):317-30 doi 10.1038/nature14248.

46. Cirillo LA, Lin FR, Cuesta I, Friedman D, Jarnik M, Zaret KS. Opening of compacted chromatin by early developmental transcription factors HNF3 (FoxA) and GATA-4. *Mol Cell* 2002;**9**(2):279-89 doi 10.1016/s1097-2765(02)00459-8.

47. Fu X, Pereira R, De Angelis C, Veeraraghavan J, Nanda S, Qin L*, et al.* FOXA1 upregulation promotes enhancer and transcriptional reprogramming in endocrine-resistant breast cancer. *Proc Natl Acad Sci U S A* 2019 doi 10.1073/pnas.1911584116.

48. Hurtado A, Holmes KA, Ross-Innes CS, Schmidt D, Carroll JS. FOXA1 is a key determinant of estrogen receptor function and endocrine response. *Nat Genet* 2011;**43**(1):27-33 doi 10.1038/ng.730.

49. Robinson JL, Hickey TE, Warren AY, Vowler SL, Carroll T, Lamb AD*, et al.* Elevated levels of FOXA1 facilitate androgen receptor chromatin binding resulting in a CRPC-like phenotype. *Oncogene* 2014;**33**(50):5666-74 doi 10.1038/onc.2013.508.

50. Tsherniak A, Vazquez F, Montgomery PG, Weir BA, Kryukov G, Cowley GS*, et al.* Defining a Cancer Dependency Map. *Cell* 2017;**170**(3):564-76 e16 doi 10.1016/j.cell.2017.06.010.

51. Glont SE, Chernukhin I, Carroll JS. Comprehensive Genomic Analysis Reveals that the Pioneering Function of FOXA1 Is Independent of Hormonal Signaling. *Cell Rep* 2019;**26**(10):2558-65 e3 doi 10.1016/j.celrep.2019.02.036.

52. Reilly JF, Maher PA. Importin beta-mediated nuclear import of fibroblast growth factor receptor: role in cell proliferation. *J Cell Biol* 2001;**152**(6):1307-12 doi 10.1083/jcb.152.6.1307.

53. McLean CY, Bristor D, Hiller M, Clarke SL, Schaar BT, Lowe CB*, et al.* GREAT improves functional interpretation of cis-regulatory regions. *Nat Biotechnol* 2010;**28**(5):495-501 doi 10.1038/nbt.1630.

54. Perera TPS, Jovcheva E, Mevellec L, Vialard J, De Lange D, Verhulst T*, et al.* Discovery and Pharmacological Characterization of JNJ-42756493 (Erdafitinib), a Functionally Selective Small-Molecule FGFR Family Inhibitor. *Mol Cancer Ther* 2017;**16**(6):1010-20 doi 10.1158/1535-7163.MCT-16-0589.

55. Lan T, Morgan DA, Rahmouni K, Sonoda J, Fu X, Burgess SC*, et al.* FGF19, FGF21, and an FGFR1/beta-Klotho-Activating Antibody Act on the Nervous System to Regulate Body Weight and Glycemia. *Cell Metab* 2017;**26**(5):709-18 e3 doi 10.1016/j.cmet.2017.09.005.

56. Oladipupo SS, Smith C, Santeford A, Park C, Sene A, Wiley LA*, et al.* Endothelial cell FGF signaling is required for injury response but not for vascular homeostasis. *Proc Natl Acad Sci U S A* 2014;**111**(37):13379-84 doi 10.1073/pnas.1324235111.

57. Ono K, Kita T, Sato S, O'Neill P, Mak SS, Paschaki M*, et al.* FGFR1-Frs2/3 signalling maintains sensory progenitors during inner ear hair cell formation. *PLoS Genet* 2014;**10**(1):e1004118 doi 10.1371/journal.pgen.1004118.

58. Zhao M, Ross JT, Itkin T, Perry JM, Venkatraman A, Haug JS*, et al.* FGF signaling facilitates postinjury recovery of mouse hematopoietic system. *Blood* 2012;**120**(9):1831-42 doi 10.1182/blood-2011-11-393991.

59. Goyal L, Saha SK, Liu LY, Siravegna G, Leshchiner I, Ahronian LG*, et al.* Polyclonal Secondary FGFR2 Mutations Drive Acquired Resistance to FGFR Inhibition in Patients with FGFR2 Fusion-Positive Cholangiocarcinoma. *Cancer Discov* 2017;**7**(3):252-63 doi 10.1158/2159-8290.CD-16-1000.

60. Pal SK, Rosenberg JE, Hoffman-Censits JH, Berger R, Quinn DI, Galsky MD*, et al.* Efficacy of BGJ398, a Fibroblast Growth Factor Receptor 1-3 Inhibitor, in Patients with Previously Treated Advanced Urothelial Carcinoma with FGFR3 Alterations. *Cancer Discov* 2018;**8**(7):812-21 doi 10.1158/2159-8290.CD-18-0229.

61. Razavi P, Chang MT, Xu G, Bandlamudi C, Ross DS, Vasan N*, et al.* The Genomic Landscape of Endocrine-Resistant Advanced Breast Cancers. *Cancer Cell* 2018;**34**(3):427-38 e6 doi 10.1016/j.ccell.2018.08.008.

62. Lee JE, Shin SH, Shin HW, Chun YS, Park JW. Nuclear FGFR2 negatively regulates hypoxia-induced cell invasion in prostate cancer by interacting with HIF-1 and HIF-2. *Sci Rep* 2019;**9**(1):3480 doi 10.1038/s41598-019-39843-6.

63. Ross-Innes CS, Stark R, Teschendorff AE, Holmes KA, Ali HR, Dunning MJ*, et al.* Differential oestrogen receptor binding is associated with clinical outcome in breast cancer. *Nature* 2012;**481**(7381):389-93 doi 10.1038/nature10730.

64. Somanathan S, Stachowiak EK, Siegel AJ, Stachowiak MK, Berezney R. Nuclear matrix bound fibroblast growth factor receptor is associated with splicing factor rich and transcriptionally active nuclear speckles. *J Cell Biochem* 2003;**90**(4):856-69 doi 10.1002/jcb.10672.

65. Fu X, Jeselsohn R, Pereira R, Hollingsworth EF, Creighton CJ, Li F*, et al.* FOXA1 overexpression mediates endocrine resistance by altering the ER transcriptome and IL-8 expression in ER-positive breast cancer. *Proc Natl Acad Sci U S A* 2016;**113**(43):E6600-E9 doi 10.1073/pnas.1612835113.

66. Lupien M, Eeckhoute J, Meyer CA, Wang QB, Zhang Y, Li W*, et al.* FoxA1 translates epigenetic signatures into enhancer-driven lineage-specific transcription. *Cell* 2008;**132**(6):958-70 doi 10.1016/j.cell.2008.01.018.

67. Li C, Iida M, Dunn EF, Ghia AJ, Wheeler DL. Nuclear EGFR contributes to acquired resistance to cetuximab. *Oncogene* 2009;**28**(43):3801-13 doi 10.1038/onc.2009.234.

68. Liccardi G, Hartley JA, Hochhauser D. EGFR nuclear translocation modulates DNA repair following cisplatin and ionizing radiation treatment. *Cancer Res* 2011;**71**(3):1103-14 doi 10.1158/0008-5472.CAN-10-2384.

69. Cordo Russo RI, Beguelin W, Diaz Flaque MC, Proietti CJ, Venturutti L, Galigniana N*, et al.* Targeting ErbB-2 nuclear localization and function inhibits breast cancer growth and overcomes trastuzumab resistance. *Oncogene* 2015;**34**(26):3413-28 doi 10.1038/onc.2014.272.

70. Stachowiak MK, Fang X, Myers JM, Dunham SM, Berezney R, Maher PA*, et al.* Integrative nuclear FGFR1 signaling (INFS) as a part of a universal "feed-forward-and-gate" signaling module that controls cell growth and differentiation. *J Cell Biochem* 2003;**90**(4):662-91 doi 10.1002/jcb.10606.

71. Loriot Y, Necchi A, Park SH, Garcia-Donas J, Huddart R, Burgess E*, et al.* Erdafitinib in Locally Advanced or Metastatic Urothelial Carcinoma. *N Engl J Med* 2019;**381**(4):338-48 doi 10.1056/NEJMoa1817323.

72. Goyal L, Shi L, Liu LY, Fece de la Cruz F, Lennerz JK, Raghavan S*, et al.* TAS-120 Overcomes Resistance to ATP-Competitive FGFR Inhibitors in Patients with FGFR2 Fusion-Positive Intrahepatic Cholangiocarcinoma. *Cancer Discov* 2019;**9**(8):1064-79 doi 10.1158/2159-8290.CD-19-0182.

73. Andre F, Bachelot T, Campone M, Dalenc F, Perez-Garcia JM, Hurvitz SA*, et al.* Targeting FGFR with dovitinib (TKI258): preclinical and clinical data in breast cancer. *Clin Cancer Res* 2013;**19**(13):3693-702 doi 10.1158/1078-0432.CCR-13-0190.

74. Nogova L, Sequist LV, Perez Garcia JM, Andre F, Delord JP, Hidalgo M*, et al.* Evaluation of BGJ398, a Fibroblast Growth Factor Receptor 1-3 Kinase Inhibitor, in Patients With Advanced Solid Tumors Harboring Genetic Alterations in Fibroblast Growth Factor Receptors: Results of a Global Phase I, Dose-Escalation and Dose-Expansion Study. *J Clin Oncol* 2017;**35**(2):157-65 doi 10.1200/JCO.2016.67.2048.

75. Hanzelmann S, Castelo R, Guinney J. GSVA: gene set variation analysis for microarray and RNA-seq data. *BMC Bioinformatics* 2013;**14**:7 doi 10.1186/1471-2105-14-7.